



## Open Archive Toulouse Archive Ouverte (OATAO)

OATAO is an open access repository that collects the work of Toulouse researchers and makes it freely available over the web where possible.

This is an author-deposited version published in: <http://oatao.univ-toulouse.fr/>  
Eprints ID: 6326

**To link to this article:** <http://dx.doi.org/10.1080/14685240903273881>  
URL: <http://www.tandfonline.com/doi/abs/10.1080/14685240903273881>

**To cite this version:**

Cathalifaud, Patricia and Godard, Gilles and Braud, Caroline and Stanislas, Michel *The flow structure behind vortex generators embedded in a decelerating turbulent boundary layer*. (2009) *Journal of Turbulence*, vol. 10 (n° 42). pp. 1-37. ISSN 1468-5248

Any correspondence concerning this service should be sent to the repository administrator: [staff-oatao@listes.diff.inp-toulouse.fr](mailto:staff-oatao@listes.diff.inp-toulouse.fr)

# The flow structure behind vortex generators embedded in a decelerating turbulent boundary layer

P. Cathalifaud<sup>a</sup>, G. Godard<sup>b</sup>, C. Braud<sup>c</sup> and M. Stanislas<sup>c\*</sup>

*<sup>a</sup>Institut de Mécanique des Fluides (UMR 5502), UPS, Université Paul Sabatier, 18, route de Narbonne, 31062 Toulouse Cédex, France; <sup>b</sup>CORIA (UMR 6614), CNRS, Site Universitaire du Madrillet, 6801 Saint Etienne de Rouvray Cédex, France; <sup>c</sup>Laboratoire de Mécanique de Lille (UMR 8107), EC Lille, CNRS, Boulevard Paul Langevin, Cité Scientifique, 59655 Villeneuve d'Ascq Cédex, France*

The objective of the present work is to analyse the behaviour of a turbulent decelerating boundary layer under the effect of both passive and active jets vortex generators (VGs). The stereo PIV database of Godard and Stanislas [1, 2] obtained in an adverse pressure gradient boundary layer is used for this study. After presenting the effect on the mean velocity field and the turbulent kinetic energy, the line of analysis is extended with two points spatial correlations and vortex detection in instantaneous velocity fields. It is shown that the actuators concentrate the boundary layer turbulence in the region of upward motion of the flow, and segregate the near-wall streamwise vortices of the boundary layer based on their vorticity sign.

**Keywords:** flow control, vortex generators, turbulent boundary layer, adverse pressure gradient, PIV, coherent structures

## 1. Introduction

Delaying or preventing turbulent boundary layer (TBL) separation in aeronautic applications (during landing or manoeuvre of an aircraft for example) leads to enhance the lift to drag ratio and thus to fuel saving and reduction of the emitted pollution. It allows also to extend the flight envelop of an aircraft. For that purpose many actuator types were explored in the last decades over many flow configurations (flat plates, ramps, bumps, ducts, airfoils, wind turbines, etc.) [3].

Among the actuators used for that purpose, the vortex generators (VGs) were found efficient to reduce and sometimes even suppress the separated region [4]. These devices generate a streamwise vortex structure which can entrain high-momentum fluid towards the wall, hence energising the TBL, increasing quantities such as wall shear stress, turbulence intensities, momentum transfer, etc. and delaying separation. The optimal device would produce streamwise vortices just strong enough to overcome the separation without persisting within the boundary layer once the flow control objective is reached. It can be either passive or active. The resulting streamwise vortices have been subjected to many studies which helped to characterise the optimal actuator parameters and the resulting mean organisation. However, too few studies were performed on the flow re-organisation due to the difficulty to get a sufficient spatial resolution in the TBL.

---

\*Corresponding author. Email: michel.stanislas@ec-lille.fr

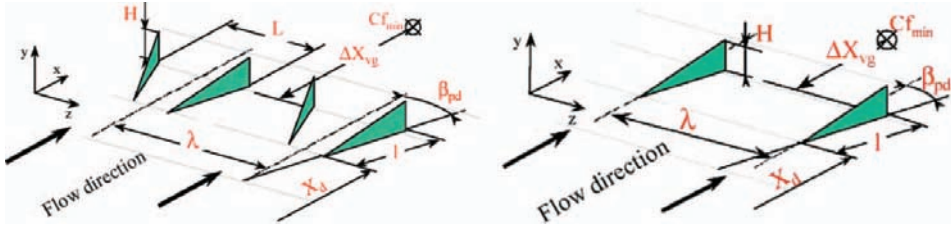


Figure 1. Geometry of counter-rotating and co-rotating passive devices.

### 1.1. Passive VGs

For passive devices, it is now well established that the strength of the vortex is driven by device parameters such as the geometry (rectangular or triangular), the height ( $h$ ) relative to the boundary layer, thickness ( $\delta$ ) and the orientation with respect to the free-stream velocity ( $\beta_{pd}$ ). When more than one device is used, the spacing between VG devices is of importance. Moreover two types of arrangements (co-rotating and counter-rotating) were found to have a rather different behaviour and thus a different control efficiency. Figures 1 and 2 give an overview of the VG parameters,  $L$  being the distance between devices of the same pair for counter-rotating arrangement and  $\lambda$  the distance between two pairs for counter-rotating arrangement or between devices in the co-rotating arrangement. The sign of the vortices produced by co-rotating and counter-rotating VGs can be seen on the mean velocity maps (see Figure 7). The co-rotating array transfers low and high momentum fluid together between the devices. The low momentum fluid being directed away from the wall and the high momentum towards the wall. The counter-rotating system dissociates the momentum transfer from the wall (upwash motion) and towards the wall (downwash motion). The high momentum is transported downward between devices of the same pair and upward between two pairs. For counter-rotating VGs, the boundary layer is thinned in the downwash area and thickened in the upwash area [5–7].

From the review of Lin (2002) [4] shapes such as rectangular plates or airfoils normal to the surface are optimal for the separation control purpose. A recent parametric exploration for a TBL over a bump configuration [1] found that delta-wings were more efficient than rectangular plates by 20% in term of skin friction gain and thus more efficient to achieve the control goal.

In the early studies, conventional VGs with a height higher or equal to  $\delta$  were first introduced [4]. However, the conventional VGs were found to produce too strong vortices which lead to a 3D organisation and additional drag compared to smaller VGs. They were rapidly replaced by smaller devices. VGs smaller than  $\delta$  and even of the order of  $0.2\delta$  (embedded in the inner log region  $y^+ < 300$ ) were still able to achieve the control of

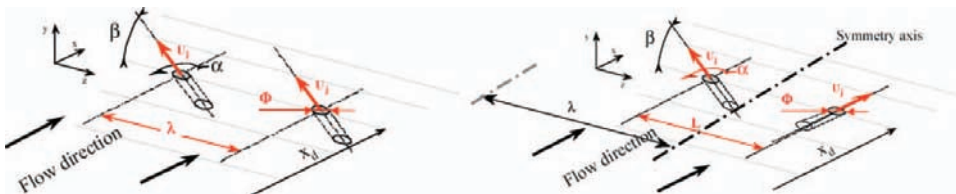


Figure 2. Co-rotating and counter-rotating round jets vortex generators configuration.

separated flows with less associated drag than conventional VGs. Off course, the streamwise lifetime of the corresponding vortices is smaller. Lin (2002) [4] suggests that these devices should be applied close to the separation region when it is relatively fixed.

The skew angle to the free stream  $\beta_{pd}$  determines the vortex strength and lateral path [8]. Tilmann et al. (2002) found that increasing  $\beta_{pd}$  generally increases the circulation and thus the control goal effectiveness. However, Godard and Stanislas (2006) [1] found by decreasing  $\beta_{pd}$  from  $23^\circ$  to  $13^\circ$  that the vortices can be linearly strengthened up. Actually, an optimum angle of attack exists which is found equal to  $\beta_{pb} = 18^\circ$  by Godard and Stanislas (2006) [1] for a bump configuration. In addition, a rapid decay of the peak vorticity downstream of the VG is observed, regardless of  $\beta_{pb}$  [1, 4, 7, 8].

For a defined flow configuration (TBL over a bump, ramp, airfoil, etc.), once the optimal  $\beta_{pb}$  is found, there exist an optimal number of devices in the spanwise direction depending on the spanwise arrangement of the VGs and the available transverse space. Godard and Stanislas [1], by measuring the downstream wall shear stress between devices of the same pair and between two pairs of counter-rotating VGs, could perform a parametric study. They found two effects when increasing the height of the device and thus the vortex circulation. In between a pair of counter-rotating VGs, the gain in term of skin friction saturates over  $h = 0.2\delta$ , whereas it still increases over  $h = 0.4\delta$  between devices of the same pair. Actually, the distance between devices, for both co-rotating or counter-rotating arrangement, is of major importance [1, 4, 5, 7]. For counter-rotating arrangements, contrary to the co-rotating ones, decreasing the transverse distance between devices was found to blow-up the vortices. On the contrary, increasing too much the spacing between devices decreases the effectiveness locally [1, 5]. Departing from a non-equidistant state ( $\lambda/L = 4$ ) Angele et al. (2005) [5] recently found, from extensive SPIV measurements, that the centres of the vortices move downstream towards an equidistant state and remain submerged in the TBL, contrary to the non-viscous theory. Therefore, the optimal spacing should be close to the equidistant state and the position of the VGs should be far enough upstream of the separation line in order for the vortices to become equidistant and to avoid back-flow in between actuators [5]. Moreover, it should be close enough to the separation line to avoid additional drag from the downstream travelling of the streamwise vortices. The optimal streamwise distance between the vortex generators line and the minimum skin friction station (or the separation line)  $\Delta X_{vg}$  is experienced to be  $\Delta X_{vg}/h < 100$ , but depending on the flow configuration (bump, ramp, airfoil, duct, etc.) [1, 4].

Note that most of the studies did not perform parametric investigations which are time consuming. The most investigated parameter is the height  $h$  of the device.

Many fundamental studies were performed to analyse the organisation of the streamwise vortices produced by VGs embedded in a zero-pressure gradient (ZPG) TBL (among others [7, 9–13]). Recent studies are addressing more realistic configurations which are streamwise vortices embedded in an APG-TBL with or without separation ([1, 5, 14] among others). Indeed the flow in which the VG is embedded influences the dynamics of the produce vortices. Viscous diffusion causes the vortices to grow, the swirling velocity component to decrease and the BL to develop towards a 2D state [5]. The adverse pressure gradient is found to promote interactions between vortices hence decreasing the control effectiveness [4]. Therefore, depending on the flow configuration (flat plate within an APG, ramp, bump, etc.) the optimal parameters vary. The main flow influence is still under investigation.

Logdberg et al. (2009) [7] have recently analysed the mean vortex path of longitudinal vortices produced by rectangular plates devices (or vane types) within a ZPG-TBL by means of flow visualisation and hot-wire measurements. This mean path is determined from the

maximum positive value of the mean velocity gradient tensor second invariant at different streamwise positions. For a counter-rotating array configuration of VGs, the vortices from the same pair first move away from each other. Thus, they move closer to the neighbouring vortex pair and eventually form a new counter-rotating pair with a common flow. Then the vortices move away from the wall. From the authors, this is due to the induced velocity in the upwash motion that tends to lift the vortices. Finally, they move again towards each other, closer to the equidistant-state. The authors attribute this last peculiar hook-like motion to the vortex growth and the limited space inside the boundary layer due to the neighbouring vortices. The maximum mean vortex radius is estimated to be  $\lambda/4$  which implies that the mean vortex centre path is within a circle defined as followed:  $y/h = 2.08$ ;  $z/\lambda = \pm 0.25$ .

Angele et al. [5] and Logdberg [14] also provide a useful rough evaluation of the vortex circulation,  $\gamma = 2khU_{vg}/\lambda$ , where  $k$  is a coefficient that depends on the device used ( $k = 0.6$  for vane-type VG in a ZPG configuration), and  $U_{vg}$  is the streamwise velocity at the tip of the device. However, this does not include the influence of the skew angle and the cross-flow organisation.

The development of SPIV measurements led to further understanding of the VGs/TBL interaction. Angele et al. (2005) [5] have recently analysed the VGs/APG-TBL interaction in terms of turbulent properties. In that study the APG induce a small separation area. They found that most of the turbulence production is locally governed by one of the gradients  $dU/dy$  or  $dU/dz$  from the S-shape profile of the streamwise velocity in the  $x$ - $y$  plane and the mushroom shape of the streamwise velocity in the  $y$ - $z$  plane. In span, between vortices, the spanwise gradient involves significant levels of turbulence production, however the flow is overall more isotropic.

## 1.2. Active VGs

Passive devices were rapidly replaced by active ones which can be turned off when not necessary in order to avoid additional drag (i.e. during cruise flight of an aircraft for instance). Many active device types were then developed for which, depending on the control source used, the control is of different nature (acoustic actuators, plasma actuators, fluidic actuators, etc.). Moreover, within fluidic actuators, one can distinguish synthetic jets devices also called Zero-Net Mass Flux [15–17] and pulsed-jet actuators [18, 19]. Indeed, for synthetic jets, contrary to pulsed-jets, there exists a suction phase. Moreover, different jet orifice shapes, orientations and operating parameters (jet oriented normal to the wall, high or low pulsating frequency, low or high velocity ratios VR between the jet exit velocity and the local free stream velocity, etc.) are used, which lead to different types of control. For instance, Greenblatt and Wagnansky [20] talk about coherent structures enhancement also called hydrodynamic control. For this control type, a low VR and a pulsating frequency adapted to the natural shedding frequency of the coherent structures is thought to be efficient. On the other hand, Raman et al. [21] are dealing with the small turbulent structures; acting on these scales is thought to allow to modify the large scale organisation more efficiently than the hydrodynamic control (no development of another dominant harmonic).

The present work is focused on control studies using fluidic actuators with addition of mass to generate streamwise vortices (also called pulsed-jets actuators or pneumatic vortex generators).

In continuous mode of the actuator, the streamwise evolution of the produced vortices by a single active device has been extensively analysed in ZPG configurations ([8, 22, 23] among others). The circulation and the associated strength of the vortex is modified by

parameters such as the ratio between the jet exit velocity and the local free stream velocity  $VR$ , the actuator pitch  $\beta$  and skew  $\alpha$  angles and the orifice shape (see Figure 2 for notations). Contrary to passive devices, the arrangement may influence significantly the produced jet, leading to additional parameters dependency. Indeed, as highlighted in Peterson et al. [24] and Warsop et al. [25], a separation occurs within the tube (or hole) due to the supply channel flow shear at the leading or trailing edge of the hole. Warsop et al. [25] found this phenomena responsible for pressure losses up to 40% at the exit, whereas Peterson and Plesniak [24] show that for low aspect ratio of the orifice exit (less than unity), the trajectory and the spanwise spreading of the exit jet can be modified depending on the sign of the ‘supply channel-inhole flow’.

Peterson and Plesniak [24] performed an extensive PIV analysis of streamwise vortices embedded in a TBL (flat plate configuration) for round jet actuators placed perpendicular to the wall. Measurements were taken in the plenum chamber and the exit hole and immediately downstream the hole. Even if the exit hole was perpendicular to the wall, this gives insight in the vortex formation mechanism. A single jet perpendicular to a wall gives rise to a pair of counter-rotating streamwise vortices, whereas two inclined jets are needed to get a qualitatively equivalent vortex pair. The origin of the remaining counter-rotating vortex pair from the jet/free stream interaction is explained by the high shear from the jet edges which induces a roll-up of the boundary layer flow. The shear is more important at the trailing edge of the hole due to bending of the jet. Behind the jet, a true wake region does not develop, but rather the action of the counter-rotating vortex pair draws the fluid away from the wall which creates a recirculation region of low velocity immediately downstream of the jet along the  $x$ -axis. When the blowing ratio increases, the jet lifts from the wall and the recirculating region is significantly reduced. Additionally, large separations occur within the exit hole of the jet which affects the following development of the two counter-rotating vortices immediately downstream the hole, when the aspect ratio of the exit hole is short (lower than 1). For instance, for a flow in the supply channel pointing in the same direction as the main flow, the counter-rotating vortices from the jet/free stream interaction are enhanced, up to 35% compared to supply channel pointing in the opposite direction to the main flow, and thus penetrates further into the TBL. Moreover, the spanwise spreading slightly decreases, when compared to supply channel pointing in the direction opposite to the main flow.

When the jet has an angle to the wall (pitch and/or skew angle), two counter-rotating vortices are initially created just downstream of the device which evolves rapidly into a single coherent vortex of one sign accompanied by a much smaller and weaker region of circulation of the opposite sign near the wall [8]. The performances increase with  $VR$  and the effect is persistent far downstream from the injection ( $\Delta X_{vg}/\Phi = 200$  or  $\Delta X_{vg}/\delta = 40$ ). For passive VGs, the primary vortex continues to move laterally in the direction of the vane skew, while for active VGs the path of the primary vortex is driven by  $VR$ . Consequently, too high jet exit velocity ( $VR$ ) can blow the vortices out of the TBL, where it is overwhelmed by the free-stream momentum and quickly dissipates, hence reducing the control effectiveness [8]. For single VGs embedded in the TBL, the vortices are similar (at least qualitatively) to the ones from passive VGs [8, 22].

Different VGs arrangements were also investigated [2]. The sign of the produced vortices from co-rotating (CO) and counter-rotating (CT) arrangements is found similar to the passive ones. The CT active VGs are found to produce similar vortices as passive ones in the same arrangement. On the contrary, CO-active VGs merge more rapidly than passive ones and thus they dissipate more rapidly. The optimal distance between devices was found 10-times smaller than for passive devices but with a higher achievable skin friction gain. For

CT actuators, the skin friction gain is proportional to VR with little skin friction gain over VR = 3.1 for a TBL over a bump configuration without separation [2]. Hence, an optimal VR exists over which the vortices may be bleed out of the TBL which wasn't observed by the authors. Logdberg [14] found that the necessary VR to achieve the control goal varies little with APG. With the assumption that for the same effectiveness criteria, the circulation is identical for both active and passive devices, a rough evaluation of the circulation  $\gamma$  for active devices was performed. Also,  $\gamma = 1.0$  to 1.5 was found enough to overcome the small separation in all three APG tested. These authors also suggest that an increase of the number of jets should be preferred to improve further the control effectiveness rather than an increase of VR (in the limit of the optimal spacing). For low VR (<4.7) and depending on the main flow configuration, the optimal skew angle is found between 45° and 90° [2, 26, 23].

The use of active VGs in the pulsed mode enables to decrease further the mass flow consumption of the actuator. Indeed, in the pulsed mode the pulsating frequency and the Duty Cycle (DC) can be tuned so that successive streamwise vortex segments can merge downstream, producing quasi-continuous streamwise vortices with less mass flow rate than the steady case [8, 19]. Also, depending on the main flow configuration (i.e. attached or separated TBL over a ramp, bump, etc.) and the actuator-jet strength (VR), the jet penetration may be modified by the pulsating frequency. Moreover, Tilmann [8] observed that pulsating the jet always generates a stronger primary vortex independently to the width of the DC. More recently, Ortmann and Kaehler, and Kostas et al. [18, 19] found a significant improvement of the control effectiveness during the first millisecond of the activation/deactivation of the actuator which was related to unsteady oscillations of the jet exit during these phases and subsequent modulation of the primary vortex strength. These oscillations were later found to be related to a wave propagation phenomena in the feeding tube of the actuator [27]. The exit jet from the fluid VG was analysed in detailed by [28]. However, this is beyond the scope of this paper which treats only the continuous mode of operation of active VGs.

These studies allow to conclude on the effectiveness of the actuator and on the mean organisation of the resulting TBL/VGs interaction. However, too little attention was paid to the TBL reorganisation behind VGs actuators. This is mainly due to the difficulty to get a good spatial resolution inside the TBL. In the present facility, the TBL is 10-times scaled-up compared to typical experimental facilities which enables to performed a more detailed analysis of the interaction between the APG-TBL and passive or active VGs. This is done using stereo PIV in different planes normal to the flow, downstream of the actuators. The mean flow and turbulent kinetic energy distributions are first characterised. Then a vortex detection analysis is performed on the instantaneous stereo PIV measurements (see Tables 1 and 2). This gives a better insight into the reorganisation of the main flow turbulence in the presence of streamwise vortices.

Parametric studies of different kinds of vortex generators were performed by Bernard et al. [29], Godard and Stanislas [1] and Godard and Stanislas [2] as part of two European projects called AEROMEMS and AEROMEMS II. The objectives were to optimise different actuator systems in order to control separation on an airfoil or a wind flap using Micro Electro-Mechanical Systems (MEMS) technology. Since such systems have very small scales, an enlargement of the scale of the phenomenon was decided to overcome the problem of spatial resolution. A stereoscopic PIV experiment was also performed by Godard and Stanislas [1] and Godard et al [32, 33].

In Section 2, the experiments performed to obtain the present database are described. In Section 3, one point statistical analysis are presented (mean velocity and turbulent kinetic

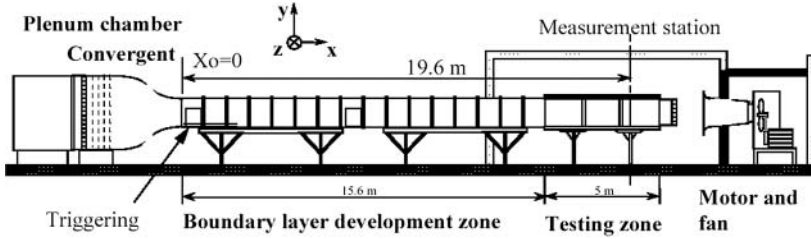


Figure 3. Front view of the TBL wind tunnel.

energy). In Section 4, the spatial correlation is analysed. In Section 5, the vortex detection method and the corresponding results are shown. Finally, a general conclusion is provided.

## 2. Description of the database

The facility used to acquire the database has the particularity to enable a TBL with  $\delta$  up to 300 mm, fully developed in the test section and characterised in the flat plate configuration by [30]. Some years ago, a bump was added within this TBL. This configuration represents the non-actuated case. A detailed analysis of this bump flow was performed by Bernard et al. [31]. Later, Godard et al. [1, 2, 32] analysed the effectiveness of different VG devices from an extensive parametric study. Gain in terms of shear stress measurements were compared and led to optimal configurations. SPIV measurements were then performed on these configurations and briefly described [33]. The same SPIV database is used in the present analysis with optimal parameters of the devices. To help the reader, some information concerning the database is recalled in this section.

### 2.1. The wind tunnel

Figure 3 is a front view of the boundary layer wind tunnel used. It is 20 m long. The last 5 m are transparent on all sides to allow the use of optical methods, and the test section is  $1 \times 2 \text{ m}^2$ . The free stream velocity for the present database was set at 10 m/s. The wind tunnel was used in closed loop to allow the use of smoke. The wind tunnel velocity is computer controlled by a PC within  $\pm 0.01\%$ ). The boundary layer under study develops on the lower wall. It is tripped at the entrance of the tunnel by a grid laid on the floor. The origin of the coordinate system is placed in the middle of the lower wall at the entrance of the tunnel. The  $x$ -axis is parallel to the wall and to the flow, the  $y$ -axis is normal to the wall, the reference frame is direct. At the beginning of the bump,  $x = 15.5 \text{ m}$ , the boundary layer thickness is  $\delta = 300 \text{ mm}$ .

### 2.2. The bump

The objective of the AEROMEMS projet was to design a bump with a pressure gradient representative of what happens on the suction side of an airfoil at moderate angle of attack and to approach separation without reaching it in order to prevent the flow to become 3D. The coordinates of the bump can be found in Bernard et al. [31]. The flow in the first half of the bump strongly accelerates with a rapid variation of the pressure gradient magnitude. At  $x = 17 \text{ m}$ , the sign of the pressure gradient changes and its variation becomes more



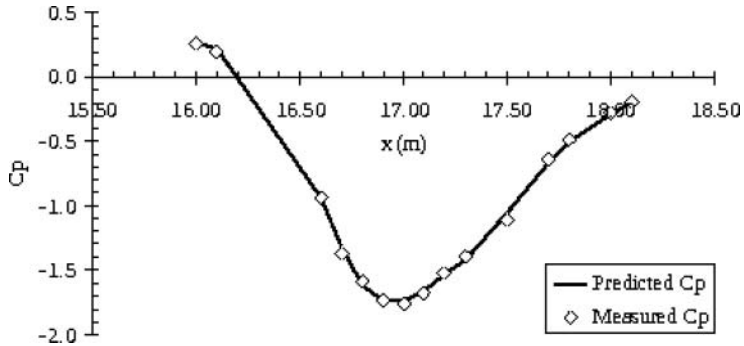


Figure 4. Distribution of the pressure coefficient over the bump.

progressive in order to avoid separation (see Figures 4 and 5). The skin friction decreases rapidly and reaches a minimum around  $x_{cfmin} = 18.58$  m.

### 2.3. The actuators

The device parameters were taken from the optimal configuration found by [1] and [2] for the same base flow. If the optimal streamwise location of the passive device was found, it was not possible, due to mechanical constraints, to place jets VGs at the same station. Active VGs were placed 0.45 m downstream of the best passive device location. However, in order to compare the active and passive actuation, measurements were also performed for a passive vortex generators array (PAb) at the same location as the round jets  $X_d = 17.55$  m.

The VGs used are:

- Passive device in the counter-rotating arrangement:
  - (1) a spanwise row of counter-rotating VGs at  $X_d = 17.10$  m (optimal streamwise location) (PA)
  - (2) a spanwise row of counter-rotating VGs at  $X_d = 17.55$  m (PAb)

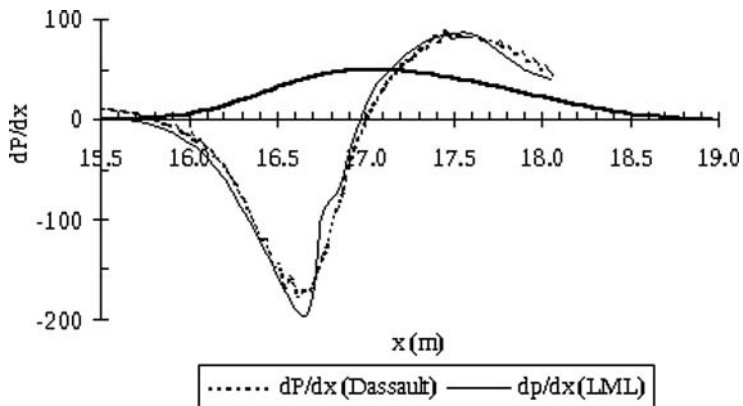


Figure 5. Distribution of the pressure gradient over the bump.

Table 1. Parameters for the passive vortex generator actuators (PA) in the counter-rotating arrangement ( $h = 26$  mm).

Type	$\delta$ (mm)	$X_d$ (m)	$h/\delta$	$l/h$	$L/h$	$\lambda/h$	$\beta_{pd}$	$\Delta X_{VG}/h$	$N_j$
PA	70	17.10	0.37	2	2.5	6	18	57	22
PAb	165	17.55	0.158	2	2.5	6	18	57	22

- Active devices at  $X_d = 17.55$  m (only in the continuous mode):

- (1) a unique pair of counter-rotating VGs (CT)
- (2) a spanwise row of co-rotating VGs (CO)

The parameters of the VG used are summarised in Tables 1 and 2:  $\delta$  is the boundary thickness without actuation at the device location,  $X_d$  is the position of the devices in the streamwise direction (see Figures 1 and 2),  $h$  is the height of the passive devices,  $l/h$  is the aspect ratio,  $\lambda$  is the transverse spacing between two devices (of the same pair in counter-rotating configurations),  $L$  is the transverse spacing between two counter-rotating pairs,  $\beta_{pd}$  is the orientation relative to the free-stream velocity,  $\Delta X_{VG} = X_{cfmin} - X_d$  is the distance between the location of the minimum friction coefficient (without actuation) and the position of the devices in the streamwise direction,  $N_j$  is the number of individual devices and VR the ratio between the jet velocity and the local free stream velocity of the base flow. The fluidic actuators are fed from a reservoir with a tube length of 200 mm and they are operating at constant pressure.

#### 2.4. SPIV measurements

A standard stereo PIV set-up was used in the configuration shown in Figure 6. It basically consists of two Nd:Yag laser cavities, each of them producing about 250 mJ per pulse at 12.5 Hz (nominal pulse frequency). The pulse duration is 5 ns. The light sheet optics consist of two lenses: one spherical to adjust the light sheet thickness (about 1 mm) and one cylindrical lens to fix the light sheet width (about 400 mm). As the main flow is going through the light sheet, a small separation, of the order of 0.5 mm, is set between the first and the second light sheets to allow a larger dynamic range.

To record the images, two PCO sensicam cameras from lavision were set on both sides of the wind tunnel in a Sheimpflug configuration. They provide  $1280 \times 1024$  pixels image pairs with 12 bits dynamic range. For the present experiments, Nikon lenses of focal length  $f = 100$  mm were used. The magnification was around  $M = 0.14$ . With an aperture of 4, the diffraction spot size was of the order of  $20 \mu\text{m}$ . The Davis software and hardware from Lavision were used for recording. The calibration was performed by recording images of a plane target at three different positions around the light sheet. Measurements were

Table 2. Parameters for the active vortex generator actuators in the counter-rotating (CT) and in the co-rotating (CO) ( $\Phi = 6$  mm).

Type	$\delta$ (mm)	$X_d$ (m)	$\Phi/\delta_l$	$L/\Phi$	$\lambda/\Phi$	$\alpha - \beta$	$\Delta X_{VG}/\delta_l$	$N_j$	VR
CT	165	17.55	0.036	15	–	45-45	7.2	2	3.1
CO	165	17.55	0.036	–	6	45-45	7.2	5	4.7

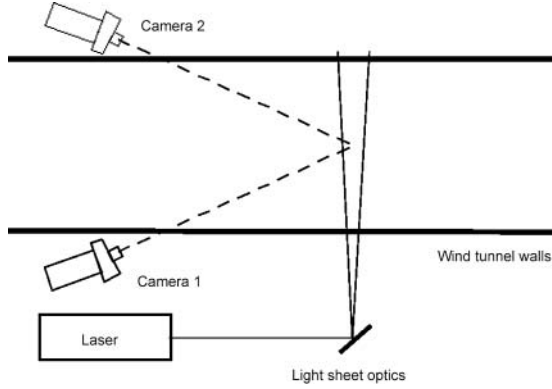


Figure 6. Scheme of the stereo PIV set-up used.

performed at three locations along the bump,  $X_{piv} = 17.67\text{ m}$ ,  $18.09\text{ m}$ ,  $18.57\text{ m}$ . The relative distance  $\Delta X_d = X_{piv} - X_d$  is given in Table 3. The measurement planes are located between the location of the actuators and the minimum of skin friction for VGs in their optimal configuration [1] and [2]. In other words, the VGs are still efficient in the last measurement plane, which is nearly at the minimum skin friction position. From now on these three stations will be respectively referred to as plane 1, plane 2 and plane 3. Note that for the PAb configuration only two downstream locations were recorded ( $\Delta X_d/h = 21$  and  $\Delta X_d/h = 40$ ).

The images from both cameras were processed with a standard multi-grid algorithm, with discrete window shifting and Gaussian peak fitting. The final interrogation window size was  $32 \times 32$  pixels with 50% of overlap. The Soloff method with three calibrations planes was used to reconstruct the three velocity components in the plane of measurement. This was done using a home-made software.

At each station, 200 instantaneous velocity maps were recorded, corresponding to 800 images of  $1280 \times 1024\text{ pixels}^2$ . In the case of the counter-rotating arrangement (both passive and active), the images were centred successively on the downwash region (PAD, PADb and CTD configurations) or the upwash one (PAU and CTU configurations). We call downwash a region where the flow is directed towards the wall, and upwash a region where the flow is ejected from the wall.

Table 3. Location of the SPIV plane measurements relative to the location of the different devices (PA, PAb, CT and CO) with  $h = 26\text{ mm}$ ,  $\Phi = 6\text{ mm}$  and  $\delta$  as the boundary layer thickness at each location of the measurement plane.

Plane	$X_{piv}$ (m)	$\delta$ (mm)	PA		PAb		CT/CO	
			$\Delta X_d/\delta$	$\Delta X_d/h$	$\Delta X_d/\delta$	$\Delta X_d/h$	$\Delta X_d/\delta$	$\Delta X_d/\Phi$
1	17.67	198	2.94	22	–	–	0.63	20
2	18.09	315	3.92	38	2.17	21	2.17	90
3	18.57	450	3.26	57	2.27	40	2.27	170

### 3. One point statistical analysis

#### 3.1. Mean velocity

##### 3.1.1. Mean velocity maps

Figures 7 to 9 give the mean velocity maps obtained at the three streamwise stations (plane 1, plane 2 and plane 3) for the three types of device: passive actuators PA (or PAb) and active counter-rotating (CT) and co-rotating (CO) devices (see Table 3). The in-plane velocity is described by the in-plane vector components, while the colour coding gives the (main)out of plane component.

#### Plane 1

At the first streamwise location (Figure 7), which was selected to characterise the vorticities just after development, the flow without actuation (WAC case) is 2D and uniform in the spanwise direction. The strong gradient region near the wall, which is still quite thin at this station, is clearly visible from the rapid colour variation at the bottom part of the map. For the actuated cases, at this station which is very near to the jets actuators, the vortices are clearly detectable for all the devices tested.

For the passive devices in a counter-rotating arrangement (PAD case), the flow resulting from the device/BL interaction leads, as expected, to two streamwise counter-rotating vortices. The centres of the vortices are located around  $[y/\delta = 0.125; \pm z/\delta = 0.25]$  or  $[y/h = 1.9; \pm z/\lambda = 0.32]$  which is in very good agreement with the location of the centres given by Logdberg [7]. In the middle of the field, a strong downwash region, induced by the two counter-rotating vortices is observed, associated with a strong streamwise velocity near the wall. At the edges of the PIV field of view, between the counter-rotating pairs, an upwash motion is observed coupled with a low streamwise velocity near the wall. Angele and Muhammad-Klingmann [5] have observed a similar inflection point configuration in the mean profiles, which is at the origin of a complex turbulent production process. As

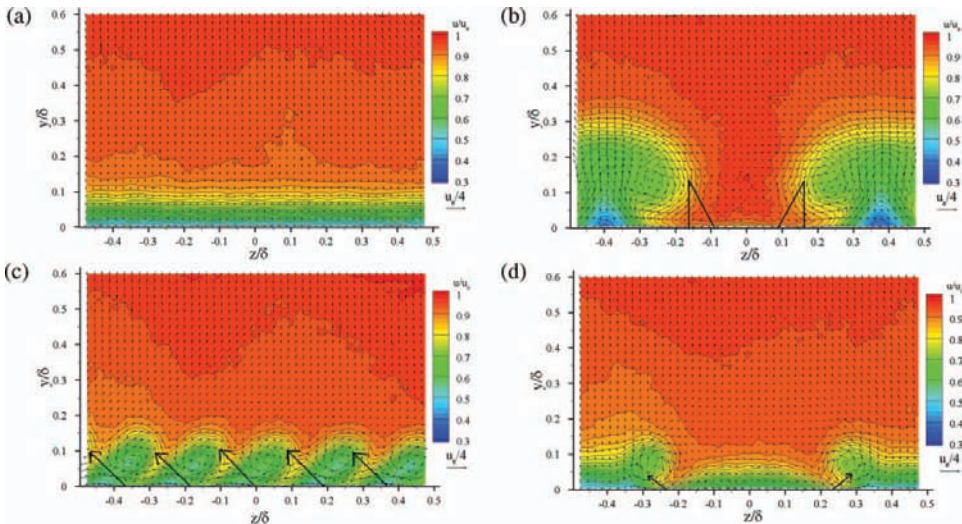


Figure 7. Plane 1: WAC, PAD, CO and CTD. The black triangular in the PAD case represents the passive devices projected on the  $y$ - $z$  plain. The Black arrows represents the jet direction from the active devices.

expected, the vortices produced by the PA actuators, which are located further upstream ( $X_d = 17.10$  m instead of  $X_d = 17.55$  m, see Table 3), are bigger in size than those due to the active devices, for which the perturbed region is two-times smaller (beneath  $y/\delta = 0.2$ ).

For counter-rotating jets, a qualitative agreement is found with passive devices. The same signs of counter-rotating vortices are found with the centre closer to the wall [ $y/\delta = 0.065$ ;  $\pm z/\delta = 0.25$ ] or [ $y/h = 0.5$ ;  $\pm z/\delta = 0.25$ ]. However, some differences are found. The mushroom-like shape is flatter than with passive devices which leads to a spreading of the structure in the transverse direction. Also, in between devices of the same pair, the streamwise velocity is weaker. This can be explained at first by the fact that in the CT case, the vortices are just developing in plane 1 while for the PA case they are fully established. Also only one pair of counter-rotating devices is used for the CT case whereas 11 pairs are used for the PA case. The second explanation is more plausible because these differences are retrieved in plane 2 where the actuators are this time at the same streamwise location.

For the co-rotating jets configuration, the flow shows a clear periodicity  $\Delta z/\delta \simeq 0.2$  of co-rotating vortices which corresponds to the periodicity of the device arrangement  $\lambda/\delta \simeq 0.2$ . A low streamwise velocity is found on each side of the jet shear area (near the wall and near the centre of the streamwise vortices).

## Plane 2

The next station ( $X_{piv} = 18.09$  m), is presented in Figure 8. The smooth wall boundary layer has clearly increased in thickness, while keeping its 2D nature. For the actuated cases, the streamwise vortices are still identifiable for the counter-rotating actuators, while they have disappeared for the co-rotating jets. The two counter-rotating devices show the same overall behaviour, with this time equivalent scale and intensity (as the PAb actuators are now at the same streamwise location as the CT ones). As expected, vortices grew in size and decreased in intensity with the growing boundary layer [4, 8, 7]. The position of the centre

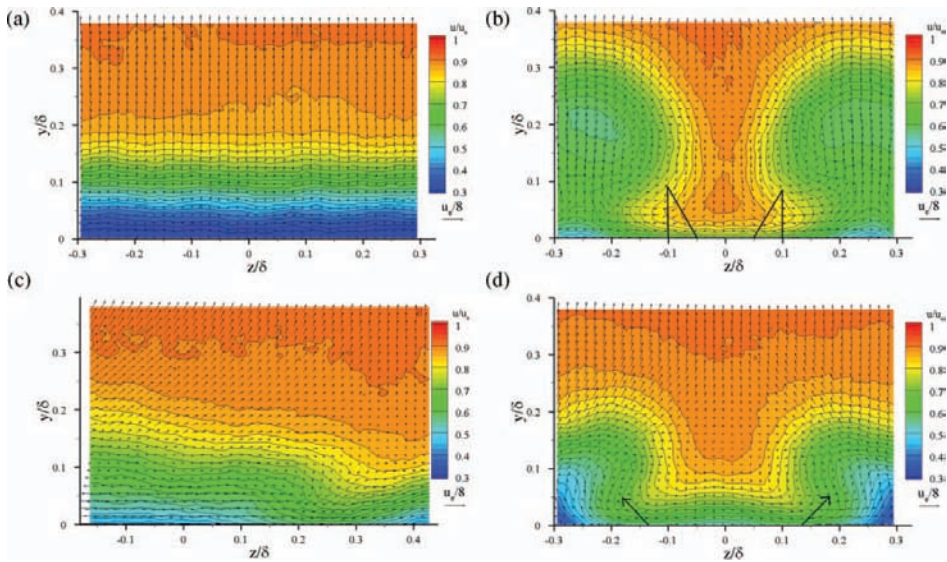


Figure 8. Plane 2: WAC, PADb, CO and CTD. The black triangular in the PAD case represents the passive devices projected on the  $y$ - $z$  plan. The Black arrows represent the jet direction from the active devices.

of vortices is approximately ( $y/\delta = 0.065$ ;  $\pm z/\delta = 0.15$ ) or [ $y/h = 0.79$ ;  $\pm z/\lambda = 0.30$ ] for both counter rotating devices, which indicates that no significant lateral movement of the streamwise vortices is observed ( $\pm z/\lambda = 0.3$  for the first two PIV plane locations). On the contrary, the vortices have moved away from the wall in the same ratio as the growth of the TBL without actuation ( $y/\delta = 0.065$  for the first two PIV plane locations). This indicates that the wall normal scaling for the mean vortex path is rather  $\delta$  than  $h$  contrary to Logdberg et al. [7]. As at the previous station, the mushroom-like shape is flatter for active devices with a weaker streamwise velocity in the very near wall region. Also, in between devices of the same pair, the streamwise velocity is weaker for the jet VGs.

For co-rotating devices, a very different behaviour is found, even if the field of view is obviously too small for this case, the wake of the VGs has turned into a region of momentum downwash towards the wall, region which has moved to the right of the figure, due to self induction of the co-rotating vortical motion near the wall. Nevertheless, the BL momentum is improved in the whole region of observation.

### Plane 3

At the last streamwise station  $X_{piv} = 18.57$  m (Figure 9), which is nearly the minimum skin friction station, the smooth wall BL has again increased in thickness. The slight transverse asymmetry should be attributed to the PIV accuracy which was a bit less in this configuration, due to some difficulties to adjust the set-up. The field of view is obviously too small for the co-rotating jets. Although some significant momentum downwash is visible, it would be interesting to assess the flow on both sides of the field of view. For the counter-rotating passive devices, the results show an homogenisation, with a streamwise velocity in the range of 0.5 to 0.7  $U_e$ , all down to the wall. The vortices trace, although fairly weak, is still detectable. The counter-rotating jets show still fairly coherent vortices. The data gives

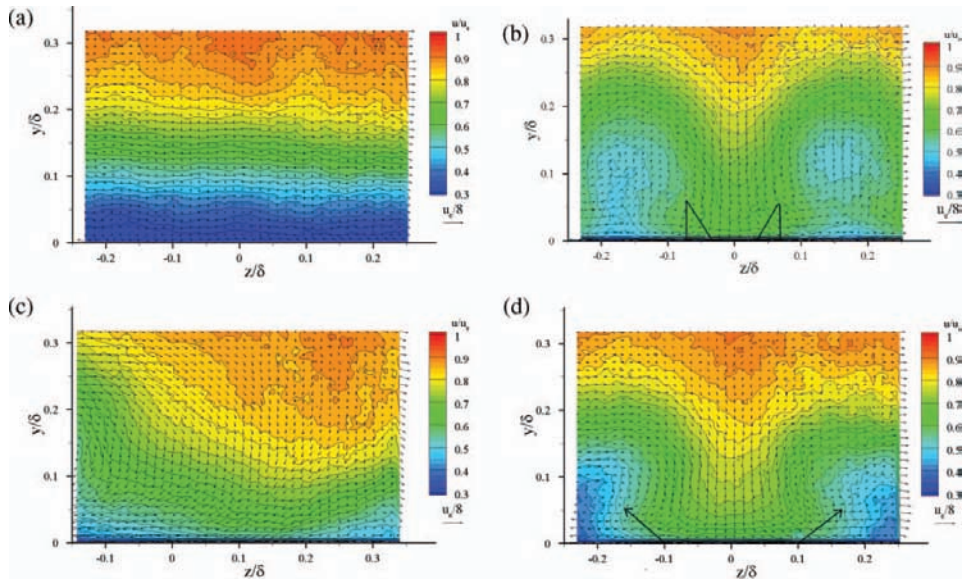


Figure 9. Plane 3: WAC, PADb, CO and CTD. The black triangular in the PADb case represents the passive devices projected on the  $y$ - $z$  plan. The Black arrows represents the jet direction from the active devices.

an evidence of alternations of low and high momentum regions near the wall, but with an increase everywhere, as compared to the smooth wall.

### Summary

For an equivalent efficiency, around 200% of shear stress gain compared to the non-actuated case (see Godard and Stanislas [2]), the PIV results in the three planes of observation evidence little differences between PA and CT and high differences between CT and CO devices. The evolution for the streamwise vortices produced by counter-rotating vortices are overall similar to the literature. The longitudinal evolution from co-rotating configuration is subject to too few studies to be compared, although Lin [4] reports it to be more efficient in 3D cross-flow configurations than in 2D configurations. In this study, the initial individual vortices are observed to merge into a large single vortical region which has the ability to globally increase the momentum near the wall.

#### 3.1.2. Mean profiles: comparison of actuator types

In addition to the above analysis on the mean field, in order to better assess the VG effect on the mean flow, some mean profiles are plotted in Figure 10 along the transverse direction  $z$ . In plane 1 ( $X_{piv} = 17.67$  m), the mean longitudinal and normal velocity profiles are given at  $y/\delta = 0.08$  for the WAC, COR, CTD and CTU configurations. In plane 2 ( $X_{piv} = 18.09$  m) and plane 3 ( $X_{piv} = 18.57$  m) mean streamwise and normal profiles are given at respectively  $y/\delta = 0.10$  and  $y/\delta = 0.22$ .

The actuation produces a noticeable transverse variation of these mean velocity components, with a different pattern depending on the type of actuation. For the PAD and CTD configuration, the mean flow exhibits an excess of streamwise velocity (compared to the WAC configuration) at the centre of the field, this excess is still clearly visible at  $X_{piv} = 18.57$  m. It appears at the left and right sides of the field in the CTU configuration. For the COR configuration, this profile, which originally exhibits 5 peaks in plane 1, evolves

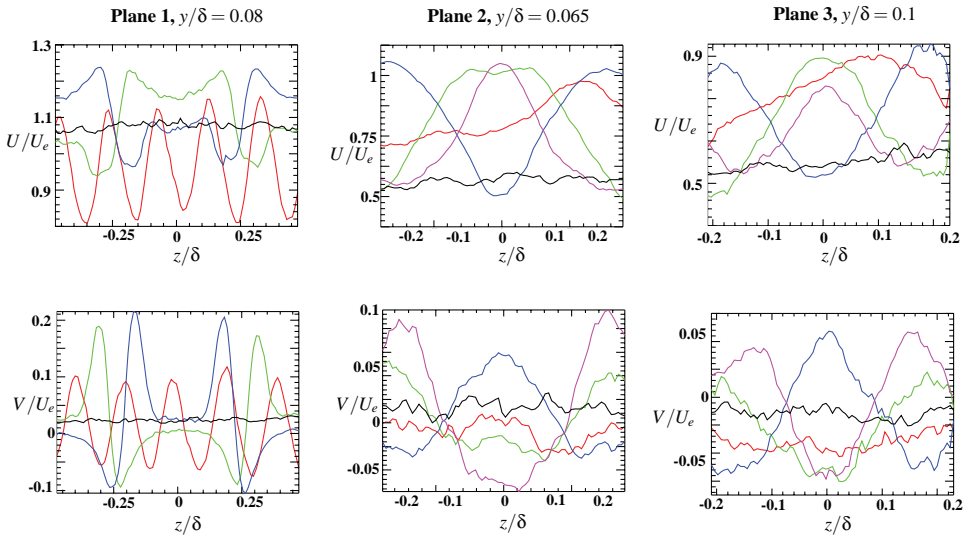


Figure 10. Profiles of the mean  $U$  (top) and mean  $V$  (bottom) in the three plane of investigation, for one wall distance and as a function of the transverse coordinate  $z$ ; WAC (black), COR (red), CTD (green), CTU (blue) and PAD (magenta) configurations.

downstream such as a global increase of the streamwise velocity is noticeable in planes 2 and 3 with a maximum around  $z/\delta = 0.25$ . In all the actuated cases, a global acceleration of the flow is observed. It can also be noticed that a maximum of streamwise velocity corresponds to a negative minimum of the normal component and a minimum of streamwise velocity corresponds to a positive maximum of  $V$  (except for the COR configuration in plane 3, where no extrema is clearly noticeable on the normal velocity profile). Actually, negative normal velocity corresponds to a transport of high-speed fluid from the free-stream. On the contrary, positive normal velocity corresponds to a transport of low-speed fluid outside the boundary layer. A clear difference in behaviour between co- and counter-rotating devices can be noticed. For the COR, in plane 1 and at the chosen altitude, a momentum deficit appears on average compared to the WAC case. This is due to the fact that the vortices are compactly staggered near the wall and leave little room between them for downwash. In planes 2 and 3, the individual vortices of plane 1 have merged together. The momentum benefit is clearly visible and the wake of the actuating device has moved transversely by self induction. For the different counter-rotating configurations, the lifetime of the individual vortices is much longer and the momentum transfer is in evident agreement with the sign and location of the different vortices. One solution to avoid the merging in the co-rotating case would be to increase the transverse spacing, but it has been shown by Godard and Stanislas [1, 2] that this reduces the overall efficiency of the device.

### 3.2. Turbulent kinetic energy

Besides the mean velocity, it is of interest to plot an indicator of the turbulence activity in the flow: the turbulent kinetic energy  $k$ . As the measurement were performed with stereo PIV, this quantity, which is half the trace of the Reynolds stress tensor is directly accessible. Figure 11 shows this quantity in the first measurement plane and for the different configurations tested. Without actuation (WAC) the turbulent activity is located, as expected, very near the wall at  $y < 0.1\delta$ . In all the actuated cases,  $k$  is enhanced significantly by the actuation and located mainly in the wake of the actuators. This indicates that the vortices

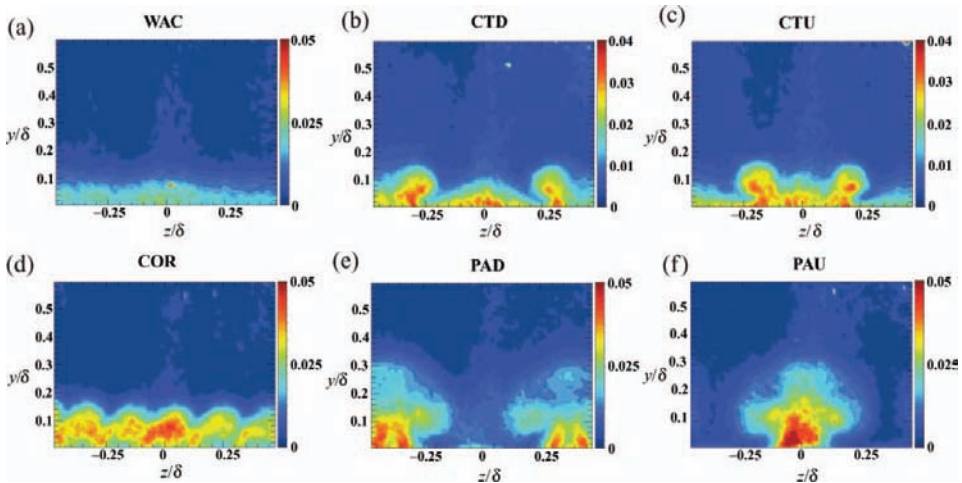


Figure 11. Turbulent kinetic energy – from top left to bottom right: WAC, CTD, CTU, COR, PAD, PAU configurations (plane 1).



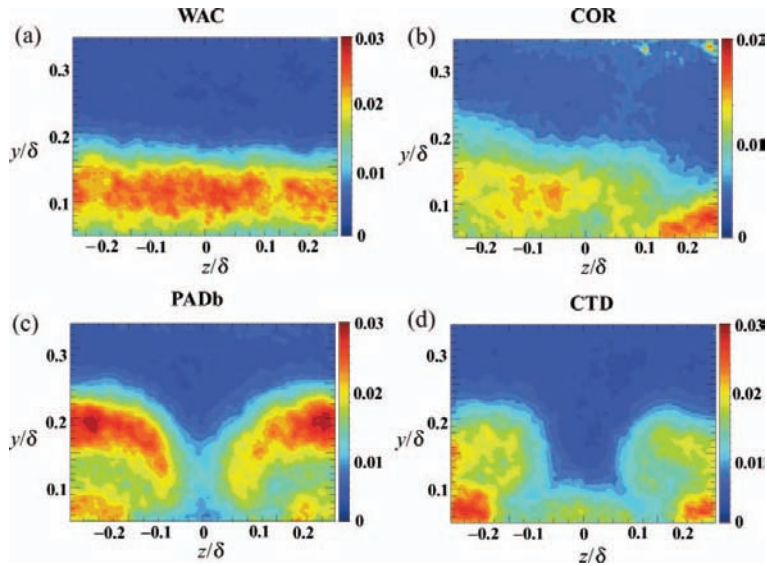


Figure 12. Turbulent kinetic energy (plane 2).

are probably slightly fluctuating in position, due to their interaction with the oncoming turbulence. In plane 2 (Figure 12), the situation has evolved significantly. First, without actuation,  $k$  has increased significantly, and the peak has moved away from the wall (in agreement with the previous HWA measurements of Bernard et al. [31]). In the actuated cases, the level of  $k$  is comparable to the WAC case and it seems that the turbulent activity has been gathered in some preferable areas of the flow. This is mainly the upwash region for the counter rotating configurations and the left part of the field, where turbulence has

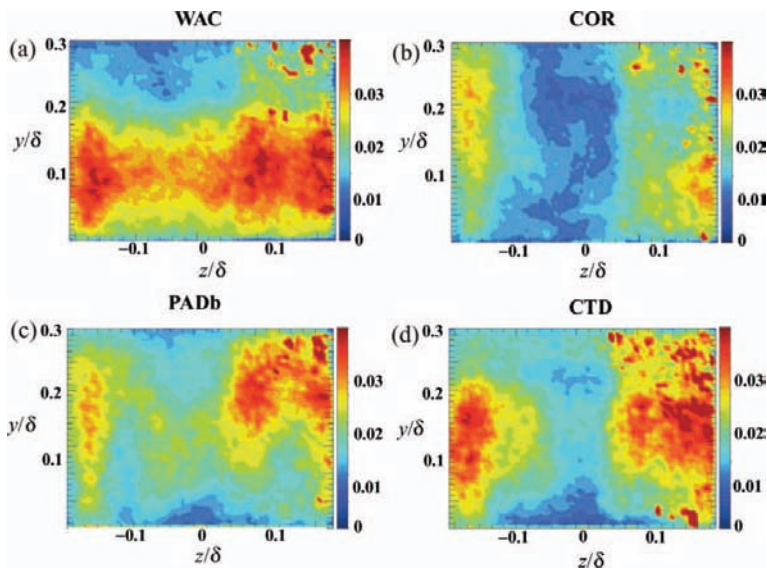


Figure 13. Turbulent kinetic energy (plane 3).

been spread as compared to the WAC case, for the co-rotating configuration. In plane 3 (Figure 13), which is far downstream (in the region of minimum wall shear stress) the turbulence peak is still intense. In the WAC case, it is wider and further away from the wall, in agreement with previous hot wire measurements [31]. The counter-rotating actuators clearly redistribute  $k$  at the top of the upwash regions. For the co-rotating case, the results are difficult to interpret.

As a conclusion, the actuators seem to generate turbulence in plane 1. This ‘apparent’ turbulence is probably due to the fluctuation in position of the vortices, as it becomes rapidly comparable in intensity to the natural one (planes 2 and 3). The actuation seems to redistribute spatially this turbulence. This is particularly evident for the counter-rotating actuators.

#### 4. Spatial correlations

Spatial correlation is classically used to reveal the underlying organisation of turbulent flows. In the present case, in order to assess the organising ability of the streamwise vortices, we have computed the two points spatial correlation of the velocity fields. The two point spatial correlation co-efficients are defined as the temporal mean value of the following relation:

$$R_{ij}(\vec{x}, \vec{d}\vec{x}, t) = \frac{\langle \vec{u}_i(\vec{x}, t) \cdot \vec{u}_j(\vec{x} + \vec{d}\vec{x}, t) \rangle}{\langle \vec{u}_i(\vec{x}, t) \cdot \vec{u}_i(\vec{x}, t) \rangle \langle \vec{u}_j(\vec{x} + \vec{d}\vec{x}, t) \cdot \vec{u}_j(\vec{x} + \vec{d}\vec{x}, t) \rangle}. \quad (1)$$

The vector  $\vec{x}$  is a two-component vector in the plane  $(y, z)$ , and it represents the coordinates of a fixed point,  $\vec{d}\vec{x}$  represents the coordinates of the moving point, and  $t$  is the time. In the present case, an ergodicity hypothesis is used: the average is not computed on time but as an ensemble average on the number of PIV maps which are supposed completely uncorrelated (this is true as the time separation between two maps is much larger than the time scale of the Taylor macro scales of the flow).

In all the results presented below, the direction normal to the wall is considered as the non-homogeneous direction. The transverse direction will sometimes be considered homogeneous. In this case, the correlation coefficients are averaged along the  $z$  direction, and the fixed point is then defined by its single wall normal coordinate  $y$ .

##### 4.1. Without actuation

First, the different spatial correlation coefficients in planes 2 and 3 in the configuration without actuation (referred to as WAC) were computed. In this particular case, the transverse direction  $z$  is considered as homogeneous. Figures 14 and 15 show these coefficients. The altitude of the fixed point is  $y/\delta = 0.065$  for plane 2 and  $y/\delta = 0.010$  for the plane 3. These altitudes correspond more or less to the centre of the vortices, when the actuators are in operation. As can be seen, the normal coefficients  $R_{22}$  and  $R_{33}$  are fairly localised, with an increase of the scales when going downstream. The wall normal velocity gradient is detectable in plane 2 on  $R_{22}$  as the correlation is computed here on the instantaneous velocities and not on the fluctuations. The cross correlation coefficients  $R_{23}$  and  $R_{32}$  show a shape which has already been observed by Bernard et al. [31] and which is typical of vortices normal to the PIV plane. Again, the size of these vortices increases downstream.

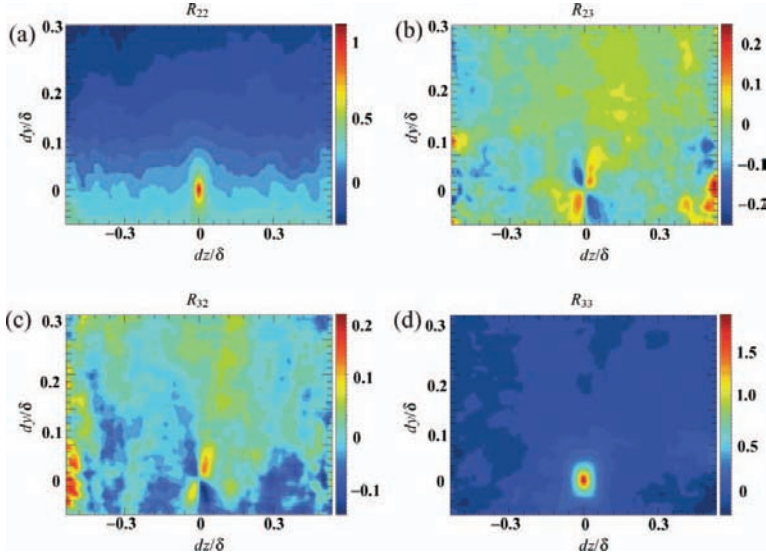


Figure 14. Spatial correlation coefficients for the configuration without actuation (WAC); plane 2; fixed point at  $y/\delta = 0.065$ .

#### 4.2. Plane 1

In this plane, only the co-rotating (COR) configuration was analysed. The fixed point is chosen at the altitude of the centre of the vortices (that is  $y/\delta = 0.077$ ). No homogeneity hypothesis is taken in the  $z$  direction. To check the transverse effect, three transverse locations of the fixed point were tested:  $z/\delta = -0.4$ ,  $z/\delta = 0$  and  $z = 0.4$ . These locations are shown in Figure 16. They correspond approximately to an analogous position compared to the first, third and fifth vortices. The  $R_{23}$  and  $R_{32}$  coefficients were computed, as they

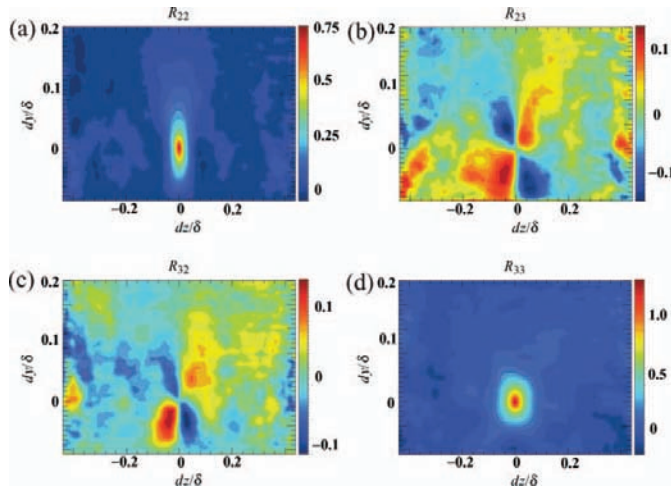


Figure 15. Spatial correlation coefficients in for the configuration without actuation (WAC); plane 3; fixed point at  $y/\delta = 0.010$ .

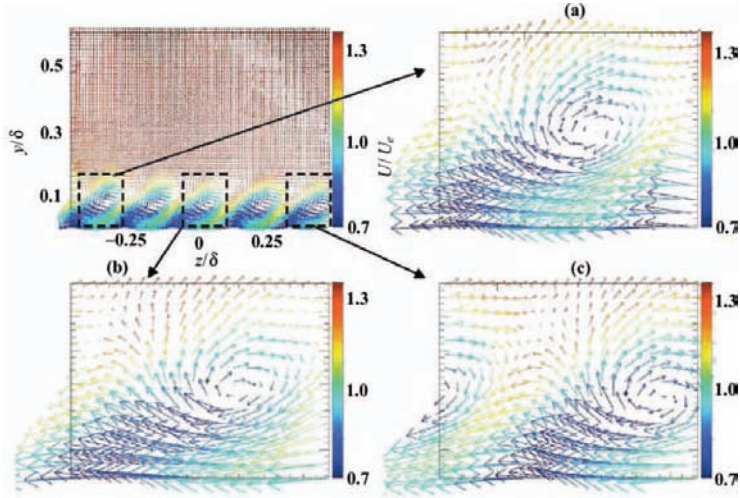


Figure 16. Mean velocity field; plane 1; COR configuration; location of the three fixed points a, b and c.

indicate the links between the normal and transverse components of the velocity. The results are shown in the Figure 17. The two coefficients show a fairly different shape. Looking first at  $R_{23}$  close to the fixed point, it shows a structure which looks like the right half of the same figure in the WAC case. This can be explained by the fact that the vortex is now located on average on the right side of the fixed point, while in the WAC case, streamwise vortices are randomly distributed. The size of the half butterfly shape is now scaled by the actuating vortices. This half butterfly is repeated periodically at each vortex location, indicating a strong transverse correlation between the vortices of the array. The  $R_{32}$  coefficient shows also a half butterfly shape near the fixed point, but this time it is the lower two lobes which are kept and which repeat themselves transversely. Curiously, the periodicity is less clear

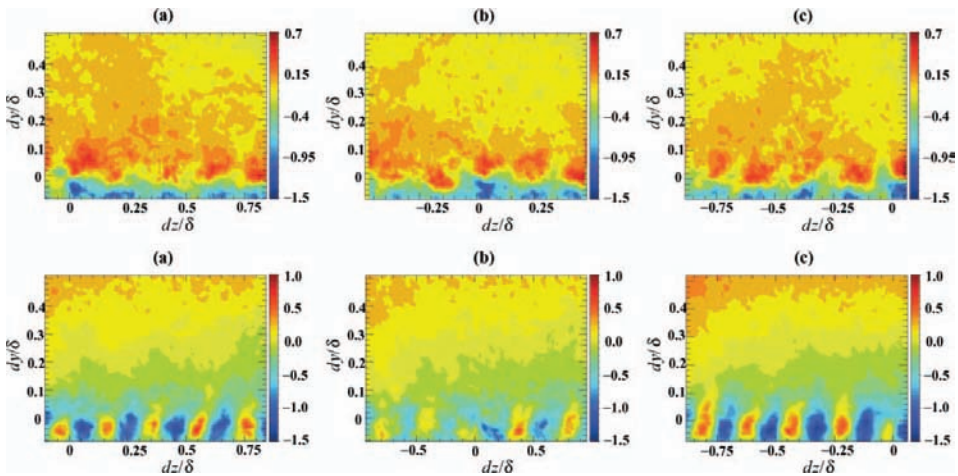


Figure 17.  $R_{23}$  (top) and  $R_{32}$  (bottom) for the three fixed point (a), (b) and (c); plane 1; COR configuration.

at point  $b$ , but this should be attributed to a lack of convergence as only 200 samples are available to compute the correlation coefficients when no homogeneity hypothesis is used. In fact a slightly better convergence could be achieved by averaging the three maps of Figure 17.

### 4.3. Plane 2

In this plane, the fixed point altitude was chosen to correspond to the centre of the vortices generated by the counter-rotating jets configuration, that is  $y/\delta = 0.065$ . First, the  $R_{23}$  coefficient was computed in the CTD, CTU and PADb configurations. The transverse direction is again considered as non-homogeneous, and the fixed point is located at  $z/\delta = 0$ . Figure 18 shows the mean velocity field with the location of the fixed point, and the corresponding iso-contours of the  $R_{23}$  coefficient in these three configurations. In the CTD and PADb configurations, at the fixed point, the mean dynamic of the flow indicates that high-speed fluid is directed towards the wall (i.e. high negative normal component of the velocity at this point), and in the CTU configuration the mean dynamic of the flow indicates that low-speed fluid is ejected from the wall towards the free-stream (i.e. high positive normal component of the velocity at this point). The butterfly shape of the  $R_{23}$  coefficient, observed in the WAC configuration (Figures 14 and 15) is clearly observable here again but with two important differences. First, in the present situation, counter-rotating streamwise vortices are existing on average on both sides of the fixed point, while in the WAC configuration single streamwise vortices of both signs are randomly distributed in the field. Secondly, the correlation pattern scales obviously here on the size of the actuating vortices which, by comparing Figures 18 and 14, appear about two-times larger than the natural streamwise structures of the TBL at this location. It must be recalled at this stage that these actuating configurations have been found optimum by the parametric study of Godard and Stanislas [1, 2]. One further point which should be noted is the fact that in the passive (PADb) configuration, the order of magnitude of the wall extrema is approximately two-times higher than in the CTD configuration. This is associated with a less noisy correlation

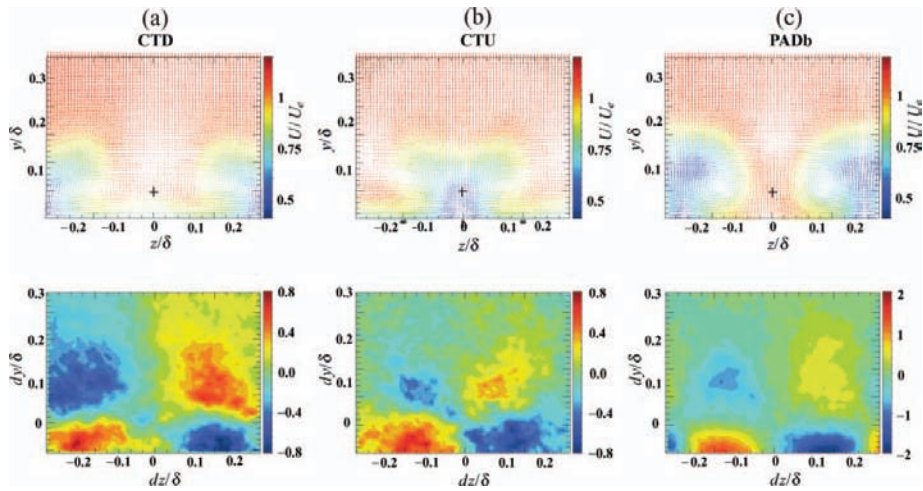


Figure 18. Mean velocity field (top) and iso-contours of  $R_{23}$  (bottom) in the CTD, CTU and PADb configurations; fixed point located at  $y/\delta = 0.065$  and  $z/\delta = 0$ ; plane 2.

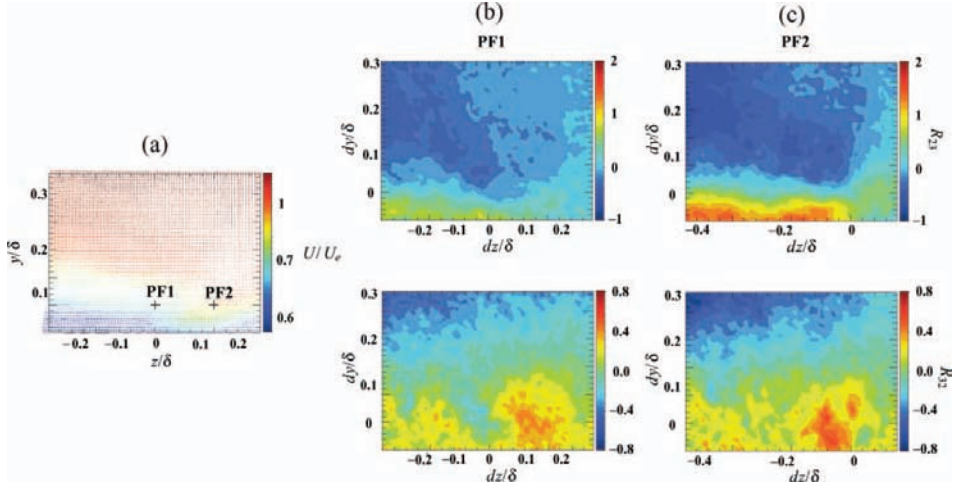


Figure 19. Mean velocity field with the location of the two fixed points PF1 and PF2 and iso-contours of  $R_{23}$  and  $R_{32}$ ; COR configuration; plane 2.

as compared to the two other cases, indicating that the BL turbulence is less affecting the actuating flow in this passive device case at this location.

In a second step, the  $R_{23}$  coefficient was computed in the COR configuration for two fixed points: one at  $y/\delta = 0.065$  and  $z/\delta = 0$  as previously (PF1), and the second one at  $y/\delta = 0.065$  cm and  $z/\delta = 0.25$  (PF2). Figure 19 shows the mean velocity field with the two fixed points and the iso-contours of the  $R_{23}$  and  $R_{32}$  coefficients for these two cases. The shape of  $R_{23}$  looks at a first glance fairly different from the counter-rotating case. A close look leads to interpret it as a single half-butterfly pattern similar to the periodic one observed in plane 1 (Figure 17) but symmetric of it. This interpretation is coherent with the existence of a large and flat clockwise vortical motion on the left part of the field (in Figure 17 the vortex was on the right side of the fixed point). This large coherent area was already interpreted by Godard and Stanislas [2] as the merging of the individual vortices identified in plane 1. The correlation is much stronger at point PF2 which is at the right border of the actuated area than at point PF1 which is in the actuated area and at the altitude where the transverse velocity component changes sign. Anyway, as in plane 1, the actuated flow shows a strong transverse correlation. As far as the  $R_{32}$  coefficient is concerned, in both the PF1 and PF2 cases, a fairly wide and significant positive peak is observed at the right of the fixed point. This can be explained by a downwash motion induced by the large vortical region located on the left of the field. The wide transverse correlation is more difficult to interpret.

Finally, the  $R_{23}$  and  $R_{32}$  coefficients were computed in the WAC, CTD, PADb and COR configurations, with  $z$  being considered as an homogeneous direction. The results are shown in the Figures 20 and 21. Apart for the co-rotating case, a strong analogy in shape is observable for both coefficient between the actuated and non-actuated cases. The size and strength vary significantly between the WAC and the actuated cases and also between the two types of actuation. The two correlation coefficients are fairly similar in size, shape and strength in the WAC case, while  $R_{23}$  shows a much stronger correlation than  $R_{32}$  for the two counter-rotating actuators. The actuating structures appear here three to four-times bigger than the natural streamwise vortices of the BL. The passive devices (PADb) induce a much

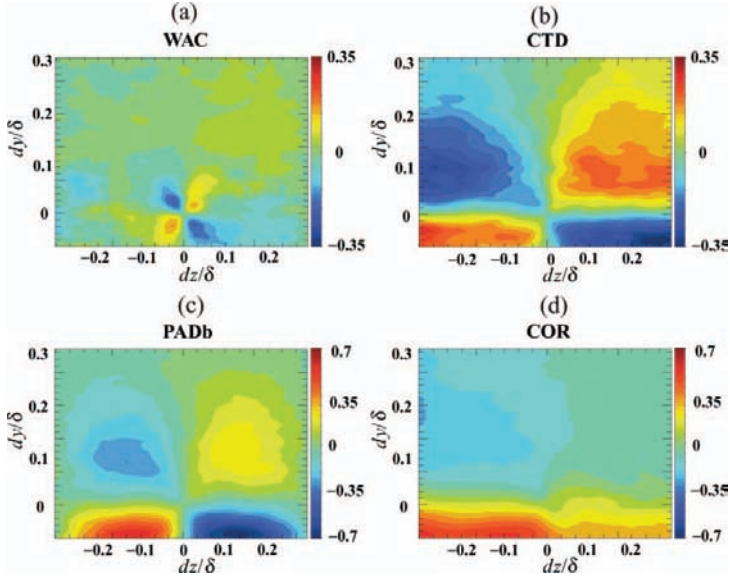


Figure 20.  $R_{23}$  iso-contours; fixed point altitude  $y/\delta = 0.065$ ,  $z$  homogeneous; plane 2.

stronger correlation than the jets system (CTD). In the co-rotating configuration (COR), the two correlation coefficients are strong too but show a fairly different shape, which is coherent with the results of Figure 19. These results clearly indicate that the counter-rotating actuation induces a mechanism which is similar to the natural one, but stronger and with larger structures while the co-rotating actuation changes significantly the boundary layer flow structure.

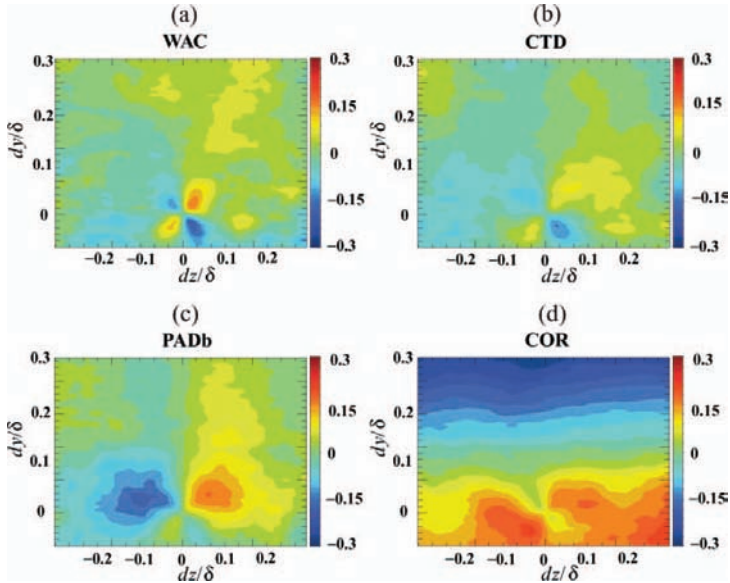


Figure 21.  $R_{32}$  iso-contours; fixed point altitude  $y/\delta = 0.065$ ,  $z$  homogeneous; plane 2.

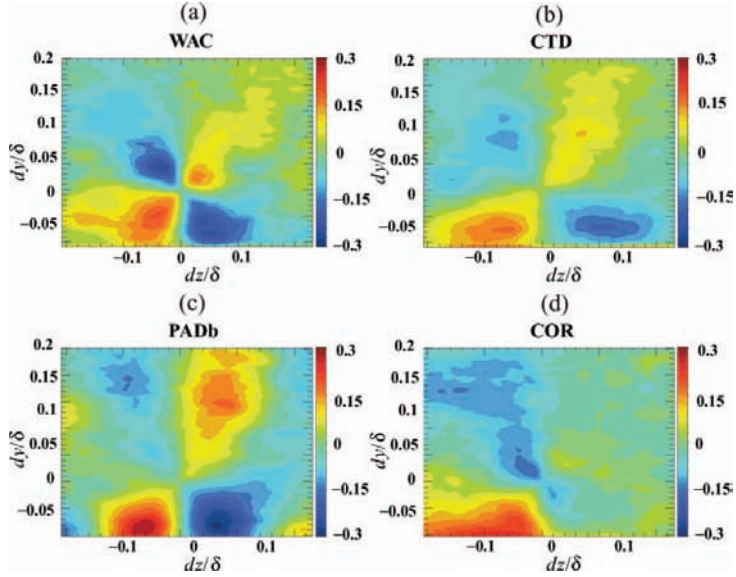


Figure 22.  $R_{23}$  iso-contours; fixed point altitude  $y/\delta = 0.010$ ,  $z$  homogeneous; plane 3.

#### 4.4. Plane 3

As previously, the fixed point altitude corresponds to the centre of the vortices generated by the counter-rotating jets configuration. This is now  $y/\delta = 0.065$ . In this plane, due to the limited number of samples, correlations computed without homogeneity hypothesis are very noisy. The transverse direction was thus considered homogeneous to compute  $R_{23}$  and  $R_{32}$ . These coefficients are shown in the Figures 22 and 23, for the WAC, CTD, PADb and

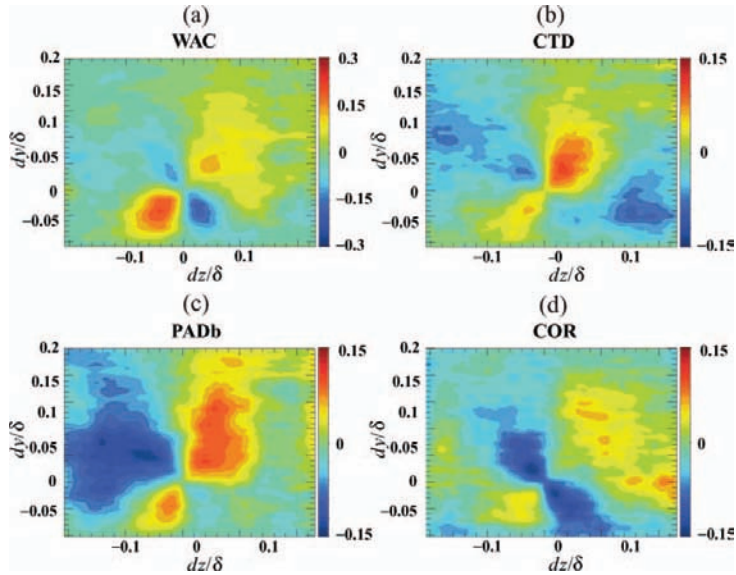


Figure 23.  $R_{32}$  iso-contours; fixed point altitude  $y/\delta = 0.010$ ,  $z$  homogeneous; plane 3.



COR configurations. They can be compared to the same data in plane 2 shown in Figures 20 and 21. Obviously, even with the homogeneity hypothesis, a larger number of samples would be of worth. As far as the shape of the correlations are concerned, the same conclusions as in plane 2 can be drawn for the counter-rotating actuators. The main difference is in the comparison of the size and strength between the actuated and non-actuated flow. They are now fairly comparable for the WAC and the CTD. The PADb being slightly stronger near the wall. Two explanations can be given to these results: either the actuating vortices have disappeared and the natural flow structures have reorganised themselves or the actuating vortices which, by comparing Figures 22 and 23 with Figures 20 and 21, appear to stay more or less constant in size, become in plane 3 of the same size as the local natural structures without actuation. Looking at the instantaneous velocity maps, the reality is somewhere in between: the actuating vortices are still present but they are mixed in the turbulent structures coming from upstream and more difficult to individualise.

## 5. Vortex detection and characterisation method

### 5.1. Detection function

Finding a reliable mathematical criterion to define a vortex is a subject which has been thoroughly addressed and which will not be discussed in detail here. Different detection functions are proposed, which are reviewed for example by Jeong and Hussain [34]. They all originate from the velocity gradient tensor  $\nabla\vec{u}$  which shows three main invariants:  $P = u_{i,i}$ ,  $Q = \frac{1}{2}u_{i,j}u_{j,i}$  and  $R = \text{Det}(u_{i,j})$ . The corresponding detection functions are:

- The enstrophy  $|\omega|^2 = |\frac{1}{2}(u_{i,j} - u_{j,i})|^2$ ; its value is related to the intensity of vortices.
- The velocity discriminant  $\Delta = (\frac{1}{3}Q)^3 - (\frac{1}{2}R)^2$ , which indicates a vortex when taking positive values.
- The second velocity invariant  $Q$ , which also indicates the presence of a vortex when taking positive values.
- The second eigenvalue  $\lambda_2$  of  $S^2 + \Omega^2$  (where  $S$  and  $\Omega$  are respectively the strain and rotation rate tensors), which takes negatives values in a vortex.

In the following,  $Q$  will be used as detection function.

All the detection functions previously defined need the use of a derivation filter. Some derivation schemes provide too noisy data, whereas other schemes have a strong smoothing effect. After testing various filters, we found that the 2nd order least square filter, which is defined as:

$$\frac{\partial u}{\partial x}(x_i) = \frac{1}{17}[u(x_i + \Delta_x) - u(x_i - \Delta_x)] + \frac{4}{17}[u(x_i + 4\Delta_x) - u(x_i - 4\Delta_x)],$$

which is the best compromise, and will be used in the following.

### 5.2. Indicative function

Having defined a detection function, a second step is to construct from it an indicative function. Usually, this is done by thresholding the detection function. This indicative function is then binary with a value of 1 at the points where the object is detected.

The difficulty here is to choose the right threshold for the detection function. We have first scaled the detection function as an 8 bits image, i.e. with values from 0 to 255. This

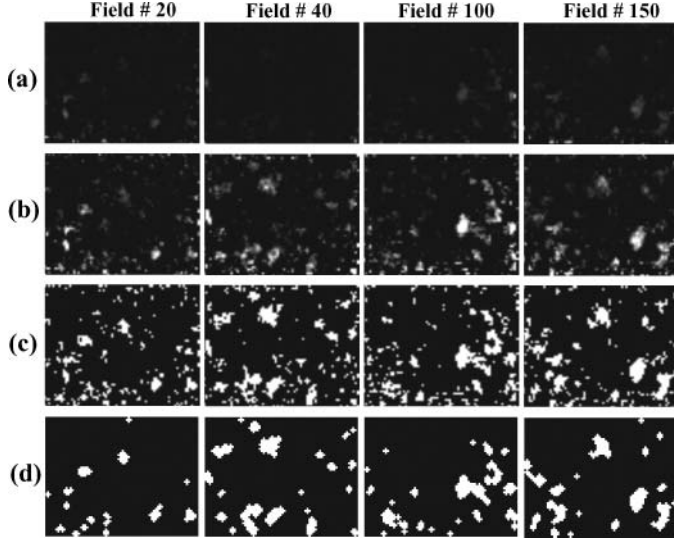


Figure 24. Vortex detection in the CTD configuration for fields number 20, 40, 100 and 150; plane 2; (a) detection function scaled between 0 and its maximum; (b) detection function scaled between 0 and  $Q_{mean}^+ + \Delta Q_{mean}^+$ ; (c) indicative function; (d) indicative function after filtering with a disc of radius 1.

was necessary to use available mathematical morphology tools. We did it in such a way that all the negative values of  $Q$  are 0 (black), and the maximum positive value of  $Q$  is 255 (white). Thus, for all the positive values of  $Q$  the grey level goes from black to white. This is illustrated in Figure 24(a) for the instantaneous field number 20, 40, 100 and 150 in the CTD configuration in plane 2. As can be seen, the images obtained are quite dark. This is due to the fact that, most often, some tiny bright peaks appear on the border of the field. We thus decided to scale the detection function differently:

- For  $Q < 0$  the pixels are clipped at 0.
- For  $Q > Q_{mean}^+ + \Delta Q_{mean}^+$  the pixels are clipped at 255, where  $Q_{mean}^+$  represents the mean value of the positive part of  $Q$ , and  $\Delta Q_{mean}^+$  is the corresponding standard deviation.

The result of this scaling is shown in Figure 24(b). As can be seen, the vortical elements are clearly evidence by this scaling.

The next step is to select the value of the threshold. Looking at a sample of fields larger than the one shown in Figure 24, it appears that a threshold  $Th \sim 8\%$  of  $Q_{mean}^+ + \Delta Q_{mean}^+$  (that is a grey level of 20 in the present case) is a good compromise between the amount of noise and the relevant vortical structures detected. Figure 24(c) shows the indicative function obtained from the detection functions of Figure 24(b) with this value of the threshold.

### 5.3. Structure extraction

The last step is the extraction of the information we want (the vortices) based on the indicative function. The binary image representation of this indicative function usually

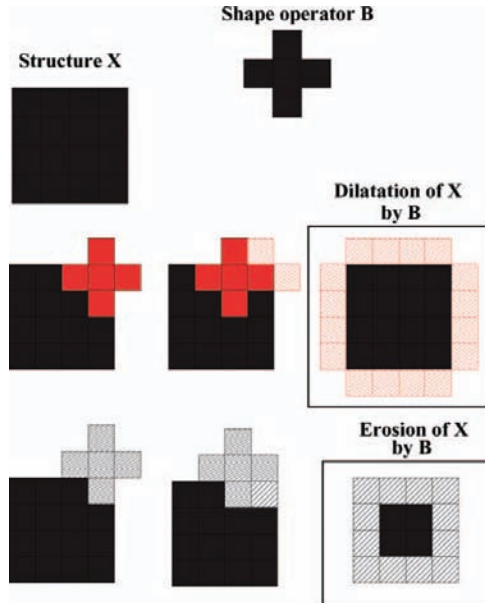


Figure 25. Example of the dilatation and erosion operations.

needs to be filtered, which may be performed using mathematical morphological functions. More information about mathematical morphology may be found in Serra [35].

As evidenced by Figure 24(c), after thresholding, noise exists in the binary images (the indicative functions) such as small structures, small holes inside structure, etc.

In order to filter this noise, morphological filters were applied. The procedure used was the following: an opening (erosion + dilatation) operator followed by a closing (dilatation + erosion) operator. The opening operation smooths the contours of the structures, cuts the narrow isthmuses and suppresses the small islands and the sharp capes. On the other hand, the closing operation blocks up the narrow channels, the small lakes and the long thin gulfs. These two operations are the combination of two fundamentals operators: erosion and dilatation. Let us consider a digital image in which there is a structure  $X$  (set of pixels equals to 1), and also consider a structuring element  $B$ . The principle of the erosion and dilatation operations are briefly illustrated with an example of  $X$  and  $B$  in Figure 25. The dilatation of  $X$  by  $B$  is the union of the black and shaded red pixels, and the eroded of  $X$  by  $B$  is the remaining black pixels.

In the present case, different structuring element were tried. The one which seemed the most convenient was a disc of radius 1, i.e. a structuring element of the following form:

$$\begin{array}{ccc} 0 & 1 & 0 \\ 1 & 1 & 1 \\ 0 & 1 & 0 \end{array}$$

Figure 24(d) shows the filtered image, obtained from the indicative functions of Figure 24(c), using the above described procedure. In order to distinguish between the positive and negative vortices, the binary images obtained were finally multiplied by the vorticity sign.

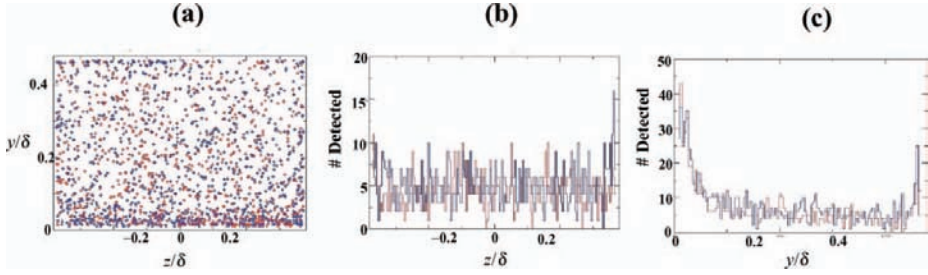


Figure 26. WAC configuration, plane 1; (a) loci of the vortex centres; (b) and (c) histograms of the number of vortex detected as a function of, respectively,  $z$  and  $y$ .

#### 5.4. Structure characterisation

The structures which remain after all the operations previously described are labelled in order to perform statistical operations on them. It is then possible to compute the average number of structures (positive and negative), the average perimeter, surface, radius, altitude, etc. The histograms of the number of structures, structures altitude and transverse positions can also be plotted. The results are presented in the next section.

### 5.5. Results

#### 5.5.1. Plane 1

In order to show the influence of jets actuation on the vortices organisation inside the boundary layer, a vortex detection was first performed for the WAC configuration. Figure 26(a) shows the loci of the vortices centres obtained by analysing the 200 velocity fields available. The red stars correspond to positive (clockwise) vortices, and the blue stars to negative (counter-clockwise) vortices. Figures 26(b) and 26(c) show the histograms of the number of vortices as a function of, respectively, the transverse and normal coordinates. The vortices are homogeneously distributed in the transverse direction, and preferably near the wall where the concentration increases strongly. Approximately four vortices of each sign were detected on the instantaneous fields, showing that the two kinds are equally probable. The average characteristics of these vortices are summarised in Table 4. These are the radius  $R$  and the intensity  $\Omega$ . The intensity is here a vorticity. The maximum (or minimum) value of the streamwise vorticity component is retained for each structure. This value is averaged over all the detected structures. The small differences between the two types of structures should be attributed to a lack of convergence. At this station, the friction velocity is  $u_\tau = 0.365$ , which gives  $R^+ = Ru_\tau/\mu \sim 73$  and  $\Omega^+ = \Omega u_\tau^2/\mu \sim 2.10^{-4}$ .

The left part of Figure 27 shows the mean velocity maps, while the right part shows the loci of the centres of the vortices detected respectively in the COR and CTD configuration. We first notice that the pattern of the vortices locations is analogous to the pattern we could anticipate from the mean velocity field (left part of Figure 27), which means that the vortices generated by the jets actuation devices (which are located just upstream this plane 1) are relatively steady. For the COR configuration, around 77% of the vortices detected are positive, and the negative vortices are located between the positive ones near the wall as shown in Figure 27. Figure 28(a) shows the histogram of the number of vortices detected as a function of the transverse coordinate. This histogram exhibits five predominant transverse locations for the positive vortex, and it also confirms that negative vortices are

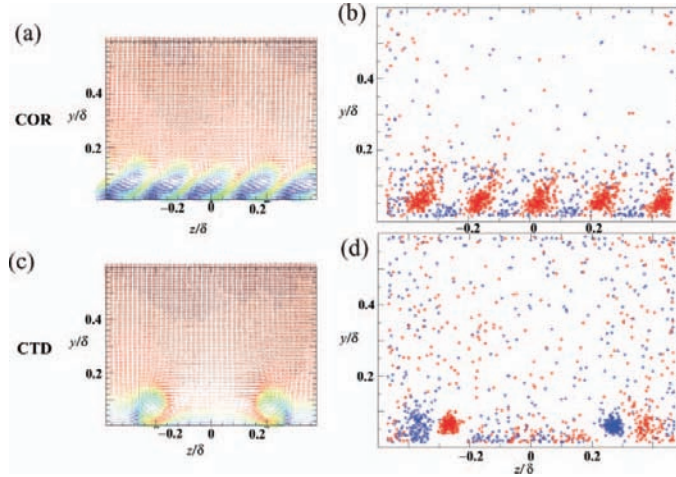


Figure 27. Mean velocity field and loci of the centres of the positive (red) and negative (blue) vortices; (top) COR, (bottom) CTD; plane 1.

dominant between these five locations. Figure 28(b) represents the histogram of the number of vortices detected as a function of the normal coordinate. The positive vortices are dominant around  $y/\delta = 0.05$ , while the negative ones show a two peaks histogram: very near the wall ( $y/\delta \sim 0$ ) and just above the positive vortices ( $y/\delta \sim 0.13$ ). The average characteristics of these vortices are summarised in the Table 4. The positive vortices have a radius almost two-times larger than the negatives ones, and their intensity is 67% higher. Both vortices are stronger than the natural ones (Table 4). The positive ones are 56% larger and the negative

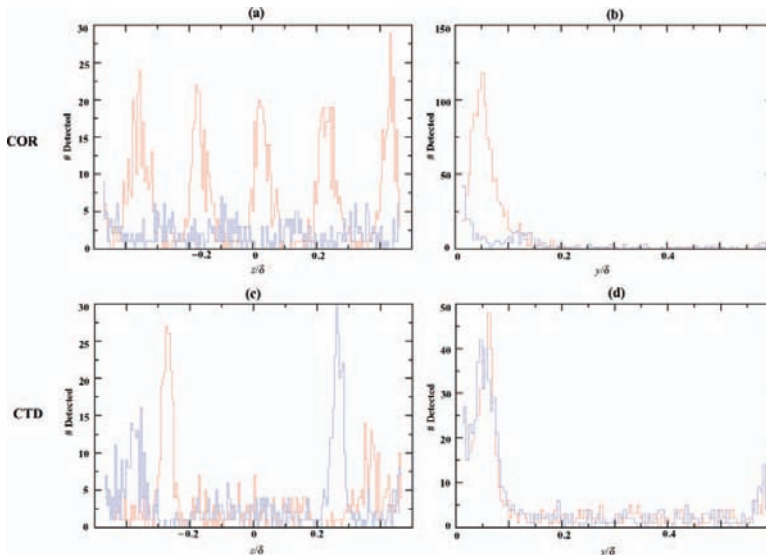


Figure 28. Histograms of the number of vortices detected (red: positive, blue: negative); (a) with respect to  $z$ ; (b) with respect to  $y$  in the COR configuration; (c) with respect to  $z$ ; (d) with respect to  $y$  in the CTD configuration; plane 1.

Table 4. Average characteristics of the vortices detected in plane 1.

Config	Features	$R$ (mm)	$\Omega$ (rad/s)
WAC	Positive vortices	2.97	1.72
	Negative vortices	3.09	-1.59
COR	Positive vortices	4.66	3.83
	Negative vortices	2.39	-2.56
CTD	Positive vortices	4.14	2.44
	Negative vortices	4.16	-2.73

ones 25% smaller. The comparison of the top two images of Figure 27, together with the value of the mean radius of the positive vortices in this case ( $R \sim 4.7$  mm) indicates that the average velocity map of Figure 27 is in fact the result of the unsteady motion of vortices which are much smaller than what this mean map indicates. The negative vortices put in evidence by the detection procedure in the right map of Figures 27 are not at all visible in the averaged velocity map. They are slightly smaller than the vortices detected in the WAC case (Table 4). They can be either secondary vortices generated in the interaction of the actuators jets with the mean flow or negative streamwise structures from the boundary layer segregated and stretched by the actuating flow. The positive ones would then be ingested by the main actuating vortices, which would explain partly their unsteadiness so near from the actuators.

For the CTD configuration (Figure 27 bottom), in addition to the two locations we could anticipate from the mean velocity field (two counter-rotating vortices), we also notice a high density of negative vortices at the left of the positive vortex, and a high density of positive vortices at the right of the negative vortex. The spatial spreading of these secondary vortices is significantly higher than that of the main ones. The histogram of Figure 28(c) confirms the existence of these two domains of vortex population close to the left and right edges of the image and around  $z/\delta = -0.24$  and  $z/\delta = 0.24$ . The altitude of both the negative vortices is around  $y/\delta = 0.05$  and a bit further for the positive vortices  $y/\delta = 0.06$  as shown in the Figure 28(d). As much positive as negative vortices were detected (three of each kind on average). Table 4 summarises their mean characteristics. We can notice the similarity between the positive and negative vortices in terms of size and intensity, which constitutes the main difference compared to the COR configuration. Here, both vortices are stronger than in the WAC case.

### 5.5.2. Plane 2

Figure 29(a) shows the loci of the centres of the detected vortices for the WAC configuration, while Figure 30 gives the same data for the COR, CTD, CTU and PADb configurations. Figures 29(b), 29(c), 31 and 32 give the corresponding histograms.

In the WAC case, the distribution is still equiprobable and homogeneous in  $z$ , but the wall region, where the population is high, has extended significantly away from the wall. This is clearly seen both in Figures 29(b) and 29(c). Table 5 gives the mean characteristics. The radius has increased by about 20% and the intensity has diminished by the same percentage as compared to plane 1. A higher concentration of positive vortices is observed in the COR configuration compared to the WAC case. These positive vortices are especially dominant on the left part of the field ( $z/\delta < 0.16$ ). The histograms of Figure 31(a)–32(a) confirm the dominance of these positive vortices in the region where the large scale motion has been

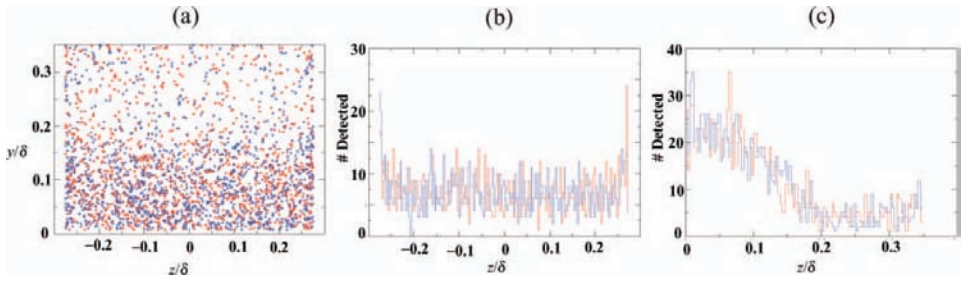


Figure 29. (a) Loci of the centres of vortices detected in the WAC configuration; (b) histogram with respect to  $z$ ; (c) histogram with respect to  $y$ ; plane 2.

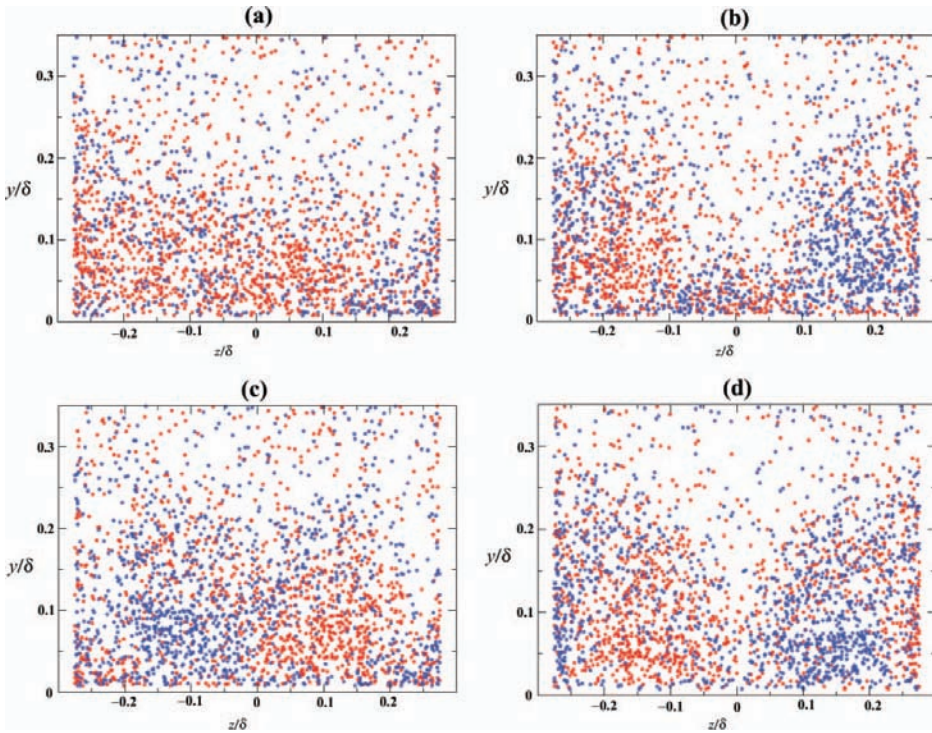


Figure 30. Loci of the centres of vortices detected (red: positive, blue: negative); (a) COR, (b) CTD, (c) CTU, (d) PADb; plane 2.

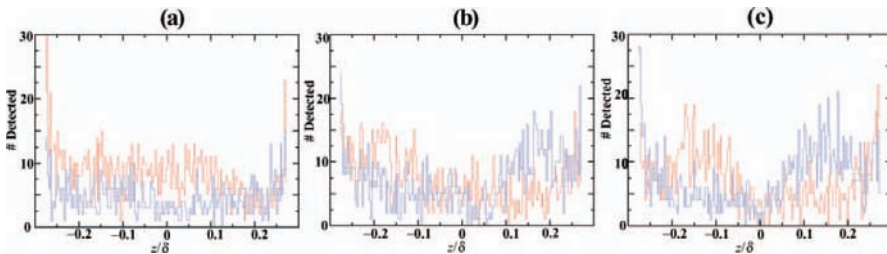


Figure 31. Histograms with respect to  $z$  of vortices detected; (a) COR, (b) CTD (c) PADb; plane 2.

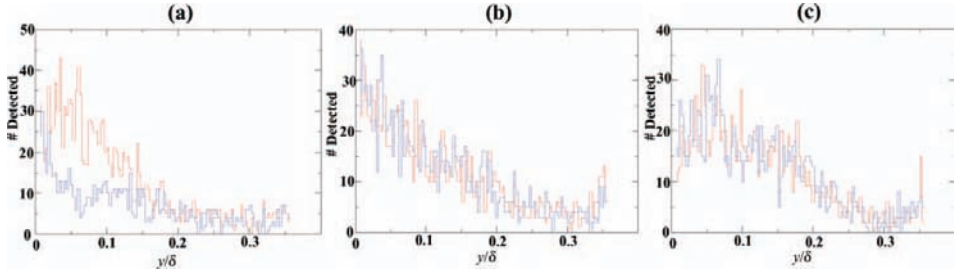


Figure 32. Histograms with respect to  $y$  of vortices detected; (a) COR, (b) CTD, (c) PADb; plane 2.

previously identified (Figure 19). In the COR configuration, we detected 75% more positive than negative vortices (about 7 positives and 4 negatives on each instantaneous field). Table 5 gives the mean characteristics of these vortices. Their intensity has significantly decreased as compared to plane 1 and is now comparable, for both signs, to the WAC case in plane 2. The positive vortices have decreased in size, while the negative ones have increased, compared to plane 1, but a difference still exists in plane 2 between both signs.

In the CTD configuration (Figure 30(b)), a concentration of positive vortices can be distinguished around  $z/\delta = -0.18$ , and of negative vortices around  $z/\delta = 0.18$  (see Figure 30(b) and Figures 31(b)–32(b)). A deficit of vortices is observed at the centre of the image, which corresponds to the downwash zone. Vortices of opposite sign gather near the wall and on each side of the origin and to a less extent, outside and above the main vortex ( $z/\delta = \pm 0.24$ ,  $y/\delta = 0.16$ ). In the CTU configuration, the opposite behaviour is obtained, with a concentration of vortices at the centre of the field (positive vortices around  $z/\delta = -0.13$  and negative vortices around  $z/\delta = 0.13$ ), which is an upwash zone, and a deficit of vortices at the left and right edges (downwash zones). The mean characteristics are given in Table 5 for the CTD and for the CTU. First, the agreement appears fairly good between the two configurations which correspond to the same flow at different transverse location. The vortices are slightly smaller than in plane 1 (about 10% on the radius) and comparable to the positive vortices of the COR case. Their intensity has decreased significantly (by about 50%) and is now comparable to that of the WAC and COR vortices.

The PADb configuration is quite similar to the CTD one (see Figures 30(d) and 31(c)–32(c)). However, it can be noticed that the transverse location of the positive vortices concentration is around  $z/\delta = -0.16$  and around  $z/\delta = 0.16$  for the negative vortices. Consequently, the downwash zone between these two concentrations is narrower than in the

Table 5. Average characteristics of the vortices detected in plane 2.

Config	Features	$R$ (mm)	$\Omega$ (rad/s)
WAC	Positive vortices	3.55	1.35
	Negative vortices	3.54	-1.39
COR	Positive vortices	3.90	1.32
	Negative vortices	3.247	-1.32
CTD	Positive vortices	3.79	1.48
	Negative vortices	3.82	-1.45
CTU	Positive vortices	3.84	1.33
	Negative vortices	3.83	-1.33
PADb	Positive vortices	4.048	1.47
	Negative vortices	4.22	-1.60



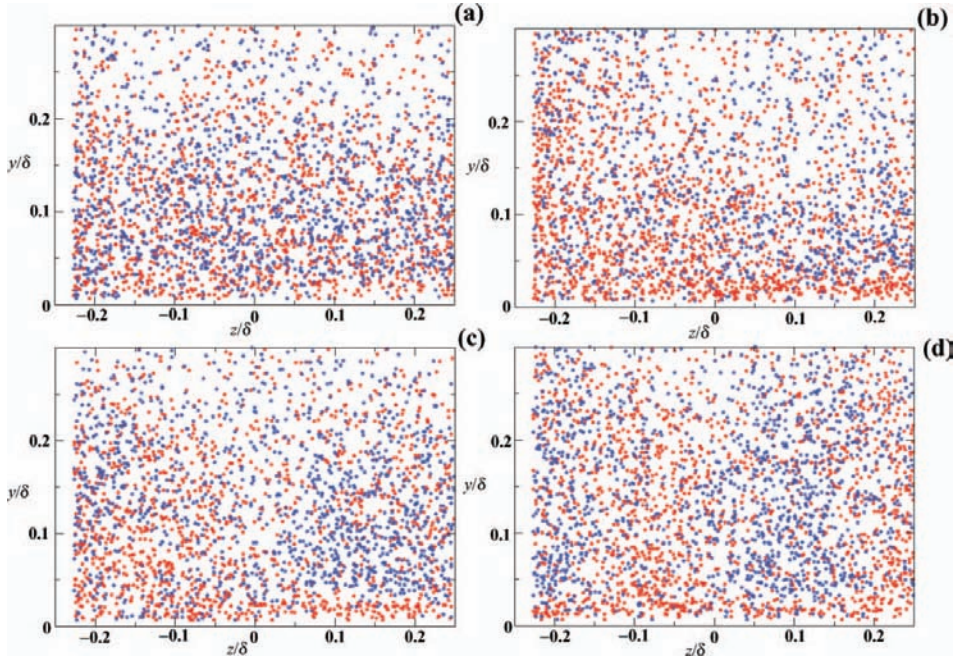


Figure 33. Loci of the centres of vortices detected (red: positive, blue: negative); (a) WAC, (b) COR, (c) CTD, (d) PADb; plane 3.

CTD configuration and the secondary counter-rotating vortices close to the wall are less numerous. The second area of secondary counter-rotating structures (around  $z/\delta = \pm 0.24$ ,  $y/\delta = 0.16$ ) is also visible.

As a summary, it can be said that although the actuating vortices still drive the global structure of the flow, the detected vortices in this plane have evolved to a size and intensity which is not far from the case without actuation. The different cases are thus distinguished mainly by the spatial distribution of the vortices of both sign, which are evenly distributed in span in the WAC case and are segregated more or less differently by the different actuators.

### 5.5.3. Plane 3

Figure 33 shows the loci of the centres of the detected vortices in the WAC, COR, CTD and PADb configurations. Their average characteristics are given in Table 6. Figure 34 shows

Table 6. Average characteristics of the vortices detected in plane 3.

Config	Features	$R$ (mm)	$\Omega$ (rad/s)
WAC	Positive vortices	5.01	1.61
	Negative vortices	4.94	-1.44
COR	Positive vortices	4.79	1.37
	Negative vortices	4.41	-1.28
CTD	Positive vortices	4.84	1.69
	Negative vortices	4.59	-1.40
PADb	Positive vortices	5.12	1.55
	Negative vortices	5.00	-1.40

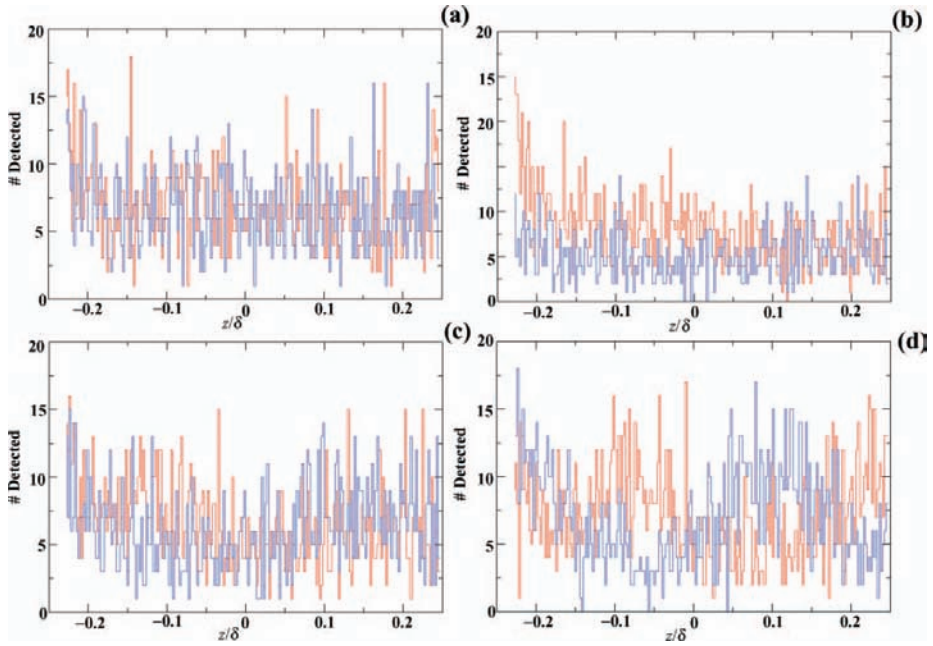


Figure 34. Histograms with respect to  $z$  of vortices detected; (a) WAC, (b) COR, (c) CTD, (d) PADb; plane 3.

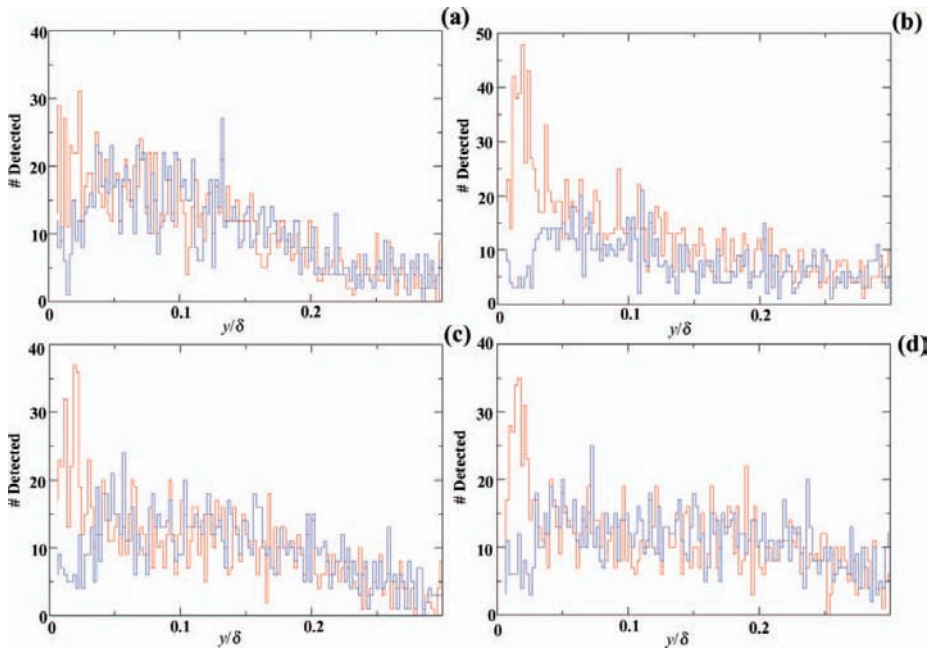


Figure 35. Histograms with respect to  $y$  of vortices detected; (a) WAC, (b) COR, (c) CTD, (d) PADb; plane 3.

the histograms of the number of vortices detected as a function of the transverse coordinate in the same configurations and Figure 35 the histograms in the wall normal direction. The differences between all four configurations are much less evident than in the first two planes. At this station, turbulent diffusion has strongly acted to distribute the vortices over the whole field of view. The WAC case is still homogeneous along  $z$ . The slight excess of positive vortices near the wall should be attributed to a lack of convergence. The vortical region is much wider than in the upstream planes. It extends now to  $y/\delta \sim 0.25$ . The two concentrations of positive and negative vortices can still be clearly distinguished in the PADb configuration (see the corresponding histogram in Figure 34). They are less evident in the CTD case. The COR configuration still exhibits an excess of positive vortices on the left part of the image. In all the actuated cases, a higher concentration of positive vortices is observed near the wall, especially in the COR configuration (see the histograms in Figure 34). Actually, for the COR configuration, 58% more positive than negative vortices are detected.

Like in plane 2, the size and intensity of the vortices in the actuated cases are comparable to the WAC configuration. The intensity of the negative vortices is slightly smaller than that of the positive ones in all cases, including WAC. This result should thus be taken with caution and attributed, for the moment, to a lack of convergence. Compared to plane 2, the size of the vortices has slightly increased, which is not surprising, but their intensity has increased too, which is more difficult to explain.

To summarise, in this plane, which is far downstream of the actuators ( $\Delta Xd/h = 57$ ,  $\Delta Xd/\Phi = 170$ ), the vortical actuating flow has strongly mixed with the boundary layer turbulence and it becomes difficult to distinguish the actuating vortices in the instantaneous velocity maps. Nevertheless, as was shown by Godard and Stanislas [1, 2], the actuation is still fairly efficient on average when looking at the wall friction.

## 5.6. Discussion and conclusion

As was shown by the above results, the analysis of the vortical structure of the flow in planes normal to the wall and to the mean flow are quite instructive on the actuating flow organisation. The streamwise vortices generated by the different actuators are initially fairly localised in space and have a size and intensity different from the boundary layer turbulence. When developing downstream, they strongly reorganise the near-wall vorticity, but they seem to fairly rapidly adapt themselves in size and intensity to the surrounding turbulence. Two explanations can be given to this observation: in a first scenario, the actuating vortices observed clearly in plane 1 reduce in size and in intensity to mix themselves with the existing turbulent streamwise eddies. In a second scenario, the actuating vortices grow rapidly in size so that they cannot be individualised in the turbulent background. But, they are strong

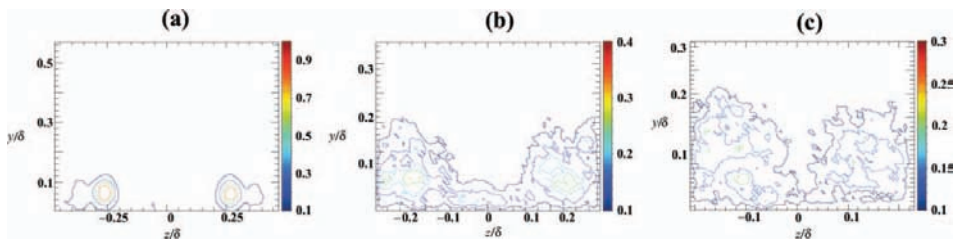


Figure 36. Mean indicative function; CTD configuration; (a) plane 1, (b) plane 2, (c) plane 3.

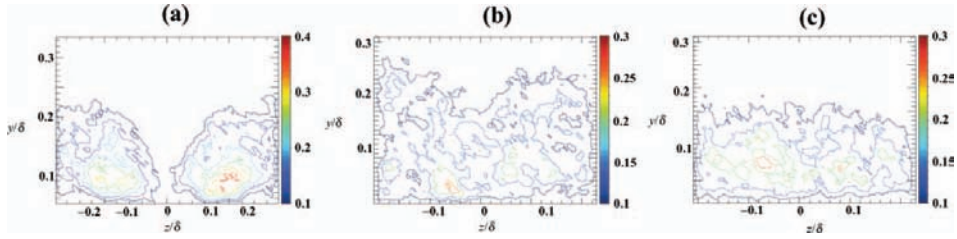


Figure 37. Mean indicative function; (a) PADb configuration, plane 2; (b) PADb configuration, plane 3; (c) WAC configuration, plane 3.

enough to organise and segregate globally the near-wall streamwise vortices of the natural boundary layer. This second scenario is somewhat supported by the results shown in Figures 36 and 37. These figures show the mean value of the indicative functions, averaged over the number of samples for the different configurations and in the different planes. This parameter is, in some way, a spatial probability of detecting a vortex. As shown by Figure 36(a), in plane 1 for the CTD configuration, this function is well localised at the place where the mean actuating vortex appears on the mean velocity map. Figures 36(b) and 37(a) show the same parameter in plane 2 for the CTD and PADb configurations. Obviously, the size of the most probable areas is much larger than the size of the individual vortices detected and comparable to the size of the average vortex evidenced in Figure 18 for example. The value of the function in the most probable area has also decreased significantly, in agreement with the spreading of the vortices location observed above. Comparable conclusion can be drawn by looking at Figures 36(c) and 37(b). The comparison of Figures 37(b) and 37(c) clearly shows that in plane 3, apart for the size of the vortical region, it becomes difficult to distinguish between the PADb and WAC cases.

## 6. General conclusion

The aim of the present study was to push further the analysis of the PIV data recorded by Godard and Stanislas [1, 2] on different actuating flow situations in order to try to better understand the physics of the flow. Measurements were available in three planes normal to the flow, downstream of the actuators and for smooth wall, passive and round jets actuators. Godard and Stanislas [1, 2] did plot only mean velocity maps out of their PIV data. In the present contribution, some mean velocity profiles were plotted to complement these maps. These profiles emphasise the difference between the co- and counter-rotating configurations and clearly show that the actuation effect is mostly due to a downwash of high momentum fluid towards the wall.

To go into more details, the turbulent kinetic energy maps were plotted, then some relevant double spatial correlation coefficients maps and, finally, the individual vortices were detected and characterised in each PIV instantaneous map. The analysis of these data confirm the difference between the co- and counter-rotating cases. With the co-rotating round jets, the actuating vortices, which are individually visible in plane 1, just downstream of the actuators, merge rapidly to form a large vortical region, which shows a global coherence on the correlation maps, which moves transversely by self-induction. This large vortical region concentrates a significant amount of turbulent kinetic energy and preferably vortices of the same sign. It shows also a global excess of streamwise velocity with respect to the non-actuated case, indicative of its efficiency. This efficiency was evidenced by Godard and Stanislas [1, 2] with wall shear stress measurements.

The counter-rotating actuators (both passive and round jets) generate stable counter-rotating streamwise vortices which stay coherent and individualised far downstream. These vortices are much stronger than the natural boundary layer vortices in plane 1 but they appear to progressively grow in size, reduce in intensity and mix themselves in the BL turbulence. They appear to segregate spatially this turbulence, concentrating the turbulent kinetic energy in the upwash regions. They also segregate the BL streamwise vortices, based on their sign, gathering them in different regions in space.

From the evolution observed in the three measurement planes, it can be expected that these actuating vortices progressively disappear downstream, but this may take a fairly long distance.

## Acknowledgements

The research reported here was undertaken as part of the AEROMEMS II project (Advanced Aerodynamic Flow Control Using MEMS, Contract No G4RD-CT-2002-00748). The AEROMEMS II project was a collaboration between BAE SYSTEMS, Dassault, Airbus Deutschland GmbH, EADS-Military, Snecma, ONERA, DLR, LPMO, Manchester University, LML, Warwick University, TUB, Cranfield University, NTUA, and Auxitrol. The project was funded by the European Union and the project partners. Part of the work was also performed in the frame of CISIT.

## References

- [1] G. Godard and M. Stanislas, *Control of a decelerating boundary layer. Part 1: Optimization of passive vortex generators*, *Aerosp. Sci. Technol.* 10(3) (2006), pp. 181–191.
- [2] G. Godard and M. Stanislas, *Control of a decelerating boundary layer. Part 3: Optimization of round jets vortex generators*, *Aerosp. Sci. Technol.* 10(6) (2006), pp. 455–464.
- [3] M. Gad el Hak, *Flow Control: Passive, Active and Reactive Flow Management*, Cambridge University Press, Cambridge, 2000.
- [4] J.C. Lin, *Review of research on low-profil vortex generators to control boundary layer separation*, *Prog. Aerosp. Sci.* 38 (2002), pp. 389–420.
- [5] K.P. Angele and B. Muhammad-Klingmann, *The effect of streamwise vortices on the turbulence structure of a separating boundary layer*, *Eur. J. Mech. B/Fluids* 24 (2005), pp. 539–554.
- [6] D. You et al., *Large-eddy simulations of longitudinal vortices embedded in a turbulent boundary layer*, *AIAA* 44(12) (2006), pp. 3032–3039.
- [7] O. Logdberg, J.H.M. Fransson, and P.H. Alfredsson, *Streamwise evolution of longitudinal vortices in a turbulent boundary layer*, *J. Fluid Mech.* 623 (2009), pp. 27–58.
- [8] C.P. Tilmann et al., *Characterization of pulsed vortex generator jets for active flow control*, RTO AVT Symposium on “Active Control Technology for Enhanced Performance Operational Capabilities of Military Aircraft, Land Vehicles and Sea Vehicles,” Germany, May 8–11, 2000.
- [9] G. Schubauer and W. Spangenberg, *Forced mixing in boundary layers*, *J. Fluid Mech.* 8 (1960), pp. 10–32.
- [10] I.M.M.A. Shabaka, R.D. Mehta, and P. Bradshaw, *Longitudinal vortices imbedded in turbulent boundary layers*, *J. Fluid Mech.* 155 (1985), pp. 37–57.
- [11] R.D. Mehta and P. Bradshaw, *Longitudinal vortices imbedded in turbulent boundary layers. Part 2: Vortex pair with “common flow” upwards*, *J. Fluid Mech.* 188 (1988), pp. 529–546.
- [12] J.K. Eaton and W.R. Pauley, *Experimental study of the development of longitudinal vortex pairs embedded in a turbulent boundary layer*, *AIAA J.* 26(7) (1988), pp. 816–823.
- [13] D.M. Rao and T.T. Kariya, *Boundary-layer submerged vortex generators for separation control – an exploratory study*, *Space Programs Technol.* 26(7) (1988), pp. 816–823.
- [14] O. Logdberg, *Turbulent boundary layer separation and control*, Ph.D. thesis, KTH Engineering science, Stockholm, Sweden, 2008.
- [15] A. Glezer and M. Amitay, *Synthetic jets*, *Annu. Rev. Fluid Mech.* 34 (2002), pp. 503–529.
- [16] K.L. Kudar and K.L. Carpenter, *Numerical investigation and feasibility study of a pzt-driven micro-valve pulsed-jet actuator*, *Flow Turbul. Combust.* 78(3/4) (2007), pp. 223–254.

- [17] C. Davies, A.A. Lockerby, and P.W. Carpenter, *Is helmoltz resonace a problem for micro-jet actuators?* Flow Turbul. Combust. 78 (2007), pp. 205–222.
- [18] J. Ortmanns and C.J. Kaehler, *Investigation of pulsed actuators for active flow control using phase locked stereoscopic particle image velocimetry*, Twelfth International Symposium on Applications of Laser Techniques to Fluid Mechanics, Lisboa, Portugal, July 12–14, 2004.
- [19] J. Kostas, J.M. Foucaut, and M. Stanislas, *The flow structure produced by pulsed-jet vortex generators in a turbulent boundary layer in an adverse pressure gradient* [Special issue on air-jet actuators and their use for flow control], Flow Turbul. Combust. 78 (2007), pp. 331–363.
- [20] D. Greenblatt and I.J. Wygnansky, *The control of flow separation by periodic excitation*, Prog. Aerosp. Sci. 36 (2000), pp. 487–545.
- [21] G. Raman et al., *Development of high bandwidth powered resonance tube actuators with feedback control*, J. Sound Vib. 269 (2004), pp. 1031–1062.
- [22] D.A. Compton and J.P. Johnston, *Streamwise votex production by pitched and skewed jets in a turbulent boundary layer*, AIAA J. 30(3) (1992), pp. 640–647.
- [23] Z.U. Khan and J.P. Johnston, *On vortex generating jets*, Int. J. Heat Fluid Flow 21 (2000), pp. 506–511.
- [24] S.D. Peterson and M.W. Plesniak, *Evolution of jets emanating from short holes into crossflow*, J. Fluid Mech. 503 (2004), pp. 57–91.
- [25] C. Warsop et al., *Pulsed air-jet actuators for separation control*, Flow Turbul. Combust. 78 (2007), pp. 255–281.
- [26] G.V. Selby, *Control of low-speed turbulent separated flow using jet vortex generators*, Exp. Fluids 12(6) (1992), pp. 394–400.
- [27] C. Braud et al., *Analysis and modelling of a fluidic actuator*, ASME Summer Heat Transfer Conference, Jacksonville, USA, August 10–14, 2008.
- [28] J. Ortmanns, M. Bitter, and C. Kaehler, *Dynamic vortex structures for flow-control applications*, Exp. Fluids 44 (2008), pp. 397–408.
- [29] A. Bernard et al., *Identification and assessment of flow actuation and control strategies*, Tech. Rep. FREP/CN18/MS001101, LML UMR 8107, Lille, France, 2000.
- [30] J. Carlier and M. Stanislas, *Experimental study of eddy structures in a turbulent boundary layer using particule image velocimetry*, J. Fluid Mech. 535(36) (2005), pp. 143–188.
- [31] A. Bernard et al., *Decelerating boudary layer: A new scaling and mixing length model*, AIAA J. 41(2) (2003), pp. 248–255.
- [32] G. Godard, J.M. Foucaut, and M. Stanislas, *Control of a decelerating boundary layer. Part 2: Optimization of slotted jets vortex generators*, Aerosp. Sci. Technol. 10(5) (2006), pp. 394–400.
- [33] G. Godard et al., *Optimization of passive and active vortex generators for boundary layer control*, Tech. Rep. AEROMEMSII/TR/LML/1.1/GG040415-1, LML UMR CNRS 8107, Lille, France, April 15, 2004.
- [34] J. Jeong and F. Hussain, *On the identification of a vortex*, J. Fluid Mech. 285 (1995), pp. 69–94.
- [35] J. Serra, *Image Analysis and Mathematical Morphology*, Academic Press, London, 1982.